A. Khanal, M. Irfan Khan, M. Fahim Shahriar, Comprehensive Parametric Study of CO2 Sequestration in Deep Saline Aquifers, Chem. Eng. Sci. (2024) 119734. https://doi.org/10.1016/j.ces.2024.119734.

Comprehensive Parametric Study of CO_2 Sequestration in Deep Saline Aquifers

Aaditya Khanal[1*], Md Irfan Khan[1], Md Fahim Shahriar[1]

[1]Jasper Department of Chemical Engineering, The University of Texas at Tyler

Corresponding author's E-mail address: aadityakhanal@uttyler.edu

A. Khanal, M. Irfan Khan, M. Fahim Shahriar, Comprehensive Parametric Study of CO2 Sequestration in Deep Saline Aquifers, Chem. Eng. Sci. (2024) 119734. https://doi.org/10.1016/j.ces.2024.119734.

Abstract

Carbon dioxide injection in deep saline aquifers is a key method for permanently sequestering anthropogenic CO_2. This study employs a reactive transport model to explore mineral precipitation/dissolution and its impact on reservoir properties in deep saline aquifers. We also assess capillary pressure and relative permeability hysteresis on various CO_2 trapping mechanisms. Results from this study reveal the significant influence of initial brine composition on mineral precipitation/dissolution. The dissolution and precipitation of minerals have different effects around the wellbores compared to the overall reservoir. Additionally, salt concentration (Ca^{++} and Mg^{++}) and quartz surface area affect CO_2 mineralization, while Na^+ impacts halite precipitation, altering flow properties. The effect of capillary pressure is significant, as including the capillary pressure in the simulation case resulted in significantly improved CO_2 trapping, achieving almost total dissolution of the injected CO_2 in around 300 years. This study offers novel insights into the interactions of reservoir minerals, brine properties, and the injected CO_2.

Keywords: Reservoir simulation, CO_2 sequestration, Mineral precipitation, Mineral dissolution, Hysteresis modeling.

1. Introduction

The atmospheric concentration of CO_2, a dominant anthropogenic greenhouse gas (GHG), which was recorded as 424 parts per million (ppm) in June 2023, has increased by almost 50% compared to the beginning of the industrial revolution [1,2]. Despite switching to renewable/low-emission energy sources and reducing CO_2 emissions by other means, global energy-related CO_2 emissions still stand at 35.5 GT, resulting in adverse climatic effects and frequent natural disasters [3–5]. The intergovernmental panel on climate change (IPCC) estimated that the earth's temperature will rise by 1.5 ^{0}C from 2030 to 2052 if CO_2 continues to increase at the current rate. Hence, there is an urgent need to mitigate CO_2 emissions and prevent the catastrophic consequences of climate change [6]. Among the CO_2 mitigation strategies, subsurface CO_2 sequestration has become one of the most promising technologies to safely sequester carbon emissions from large stationary sources and slow atmospheric CO_2 concentrations [7].

Viable geo-sequestration sites have geophysical conditions suitable for the injected CO_2 in the supercritical phase, which occurs at pressure and temperatures greater than 7.38 MPa and 304.13 K, respectively [7]. At supercritical conditions, CO_2 exists as a supercritical fluid with a liquid-like density and gas-like mobility and compressibility. The high-density of supercritical CO_2 makes it possible to store a large quantity of CO_2 in the pores initially occupied by formation fluids. Following CO_2 injection into any subsurface storage sites, initial trapping mechanisms are physical (hydrodynamic or structural trapping and residual trapping), whereas chemical-based trapping (dissolution trapping and mineral trapping) mechanisms come into effect as time progresses [8]. Upon subsurface injection, the CO_2 displaces brine from the pore spaces of the reservoir. As the density of the supercritical CO_2 (200-800 kg/m^3) is considerably lower than the brine density (950 - 1250 kg/m^3), most of the CO_2 rises upward within the aquifer until it reaches an impermeable horizontal caprock, acting as a geological seal, where it is structurally trapped as a gas or supercritical fluid beneath the aquifer caprock [5]. The supercritical CO_2 can spread laterally over a large area, depending on its buoyancy, the aquifer's shape, and the slope of the caprock until it experiences another vertical trap. Correspondingly, during residual trapping, CO_2 remains trapped as disconnected ganglia within the pore spaces of a geologic formation due to the snapping off of the continuous non-wetting phase (CO_2) [9]. Meanwhile, the buoyant CO_2 in contact with brine at the caprock slowly dissolves by molecular diffusion, forming a brine-CO_2 solution. This solution is slightly denser than the pure brine by a factor of 0.1 - 0.2 %, depending on conditions in the aquifer, where the density gradient between the top layer and the layer immediately below creates a buoyant instability, resulting in the CO_2-rich layer sinking to the bottom of the aquifer and being replaced by fresh brine. This process creates a loop, migrating the free CO_2 trapped as a separate phase to the bottom of the aquifer as the brine-CO_2 solution, known as dissolution trapping [7]. Finally, CO_2 can engage in direct or indirect reactions with rock minerals and aquifer ions in the geologic formation, resulting in the precipitation of various carbonate minerals depending on the initial brine properties and rock mineralogy. The mineral trapping process can potentially immobilize CO_2 for extended periods, impeding its release into the atmosphere.

Although several CO_2 subsurface storage sites, such as depleted oil and gas reservoirs, can store CO_2 using the same mechanisms for trapping hydrocarbons, deep saline aquifers offer significantly larger storage capacity, and suitable formations are available globally [5]. Upon injection into saline aquifers, CO_2 dissolves into its aqueous phase, forming ionic species such as HCO_3^-, CO_3^{2-} and H^+ which alters the pH, leading to several geochemical reactions such as precipitation and dissolution of minerals when interacting with carbonate and silicate minerals in the host rock. Furthermore, mineral dissolution is enhanced under acidic conditions, leading to accelerated breakdown, while alkaline conditions promote the precipitation of carbonate compounds [10]. While injecting large volumes of under-saturated (dry) supercritical CO_2 into a saline aquifer, the formation water will evaporate, increasing the molar fraction of water in the CO_2 stream. The water vaporization also leads to an increase in the concentration of NaCl in brine. Once the NaCl concentration exceeds its solubility limit, it will precipitate out as halite from aqueous phase, as shown in **Figure 1**. Moreover, the CO_2 plume spreading through the reservoir causes a decrease in pressure and an increase in temperature, leading to changes in the solubility of other minerals [9,11]. Additionally, the CO_2-saturated water has a low pH (3-4), which can dislodge fines and dissolve intergranular cement, further migrating under the drag force of the injected CO_2 and accumulating in pore throats, reducing the reservoir porosity and permeability, as illustrated in **Figure 1** [12,13]. This can cause problems during the injection process, as it reduces the storage space for CO_2 and can lead to decreased injectivity and increased operating costs, as reported in several experimental and simulation studies [8,9,11,14]. The newly formed mineral compounds generally reduce the porosity and permeability than the original rock matrix. Therefore, the precipitation of the mineral near the caprock creates a more impermeable layer underneath it, acting as a physical barrier preventing the upward migration of CO_2 [15]. This sealing effect helps to ensure the long-term containment and stability of the stored CO_2 within the targeted storage formation.

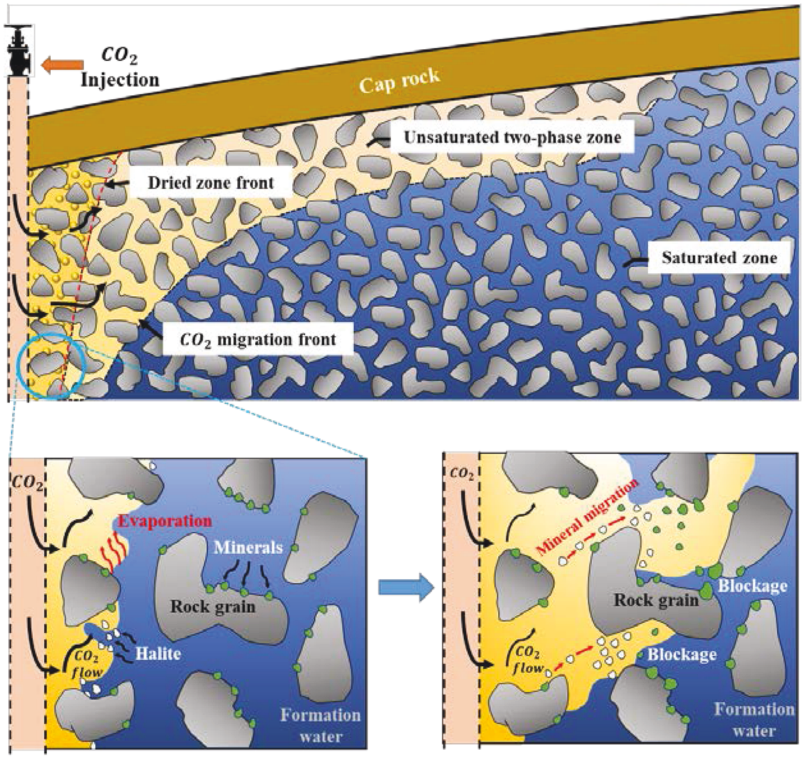

Figure 1. Evolution of mineral precipitation, migration, and retention process near the wellbore during CO_2 injection (top) and magnified view of the wellbore region (bottom)

Several recent experimental and simulation studies have been conducted to investigate the petrophysical changes during CO_2 subsurface sequestration. Xiao et al. [16] indicated that maximum porosity reduction (~ 25%) occurred at the interface between the reservoir and caprock due to mineral precipitation, resulting in enhanced caprock sealing capacity in the presence of mineral precipitation. Similar results were reported by Mohd Amin et al. [17], where the injection of CO_2 led to a decrease in caprock porosity, resulting in an enhanced sealing ability. Ilgen et al. [18] observed limited mineralization in shales following CO_2 injection. However, the study highlighted substantial calcite dissolution, facilitating dolomitization and potentially enhancing long-term storage capacity. Shiraki and Dunn [19] found a decrease in permeability due to the precipitation of kaolinite and anhydrite while examining the geochemical interaction between CO_2 and sandstone. Sayegh et al. [20] conducted CO_2 flooding experiments on sandstone cores and observed an initial decrease in permeability attributed to the migration of fine illite particles. A comprehensive investigation by Carroll et al. [21] on Mt. Simon Sandstone sample under CO_2 storage conditions (51 °C and 195 bar) revealed that the formation of Fe-carbonates, clays, and hydroxides could potentially impact the permeability of both the reservoir and seal by clogging pores and fracture networks. Liu et al. [22] investigated the effects of CO_2 sequestration in the Mount Simon. The injected CO_2 created an acidified zone (pH 3-5), resulting in extensive secondary mineral precipitation and feldspar dissolution. The study indicated a potential increase in porosity (1%) but did not report the exact change in net permeability. Initial saline aquifer properties are another dictating parameter in controlling the mineral dissolution/precipitation behavior. Edem et al. [23] conducted core flooding experiments on Grey Berea sandstone with different salinities (5, 15, 25, wt.% NaCl) and concluded that with the increase in salinity, porosity increased from 0.75% to 6%, while permeability increased from 10% to 70%. Babaei [24] investigated the impact of brine salinity and salt precipitation in reservoirs with varying boundary conditions and well patterns and reported that increasing the number of wells can significantly reduce the maximum amount of mineral precipitated.

Giorgis et al. [25] investigated the occurrence of salt precipitation during CO_2 injection in depleted gas reservoirs using TMGAS. Their findings suggested that a concentration of halite precipitation occurred near the injection well when the water saturation was above the irreducible water saturation level.

Inputs such as relative permeability curves, capillary pressure curves, and hysteresis modeling are crucial parameters in reservoir simulation [26–29]. Parvin et al. [30] developed an empirical formula describing the effect of capillary pressure on the mineral precipitation near the injection well. Their model showed that mineral precipitation occurred even in the absence of capillary pressure, but the extent of precipitation was strongly influenced by capillary pressure. Miri et al. [31] concluded that gas-liquid capillary pressure significantly affects mineral precipitation. Juanes et al. [32] reported that modeling relative permeability hysteresis is crucial to assess the amount of CO_2 immobilized by capillary trapping accurately. However, the results remained the same regardless of whether hysteretic or non-hysteretic capillary pressure curves were utilized. A similar trend was exhibited in the work of Ershadnia et al. [9], where the impact of capillary pressure on snap-off trapping was highly dependent on whether relative permeability is hysteretic or non-hysteretic. The findings reveal that when relative permeability lacks hysteresis, the proportion of CO_2 trapped through snap-off is minimal, amounting to just 1.6%.

Despite the substantial number of recent studies on trapping CO_2 in saline aquifers, based on the literature review and the authors' knowledge, some focus areas have received limited attention, as shown in **Table 1**. We summarize the focus areas explored in the prior studies but require further investigation to understand critical aspects and address knowledge gaps. Furthermore, a broad overview is provided considering the crucial factors governing CO_2 storage performance, which will provide important insights into overall saline aquifer system behavior.

Table 1. Research areas of CO_2 trapping in saline aquifers that require further investigation

Focus area	Detailed information on the contribution of this work	Sections	Prior Studies
Capillary pressure and relative permeability hysteresis effects on different trapping mechanisms	Although the short-term impact of capillary pressure and relative permeability hysteresis has been investigated for residual trapping mechanisms, its long-term implications for dissolution and mineralization are unclear.	Section 3.1.3	[33–38]
Halite precipitation	Although halite precipitation near the injection well is reported in most studies, the overall dissolution/precipitation behavior throughout the aquifer needs further investigation.	Section 3.1.4	[23,30, 39,40]
Variability in operating and geophysical parameters	Although several studies report a range of values for different parameters used in their studies, detailed investigative analysis on the effect of varying operating (injection rate) or geophysical (permeability, porosity) parameters need further investigation	Section 3.2	[33,35, 36]
Initial aquifer brine concentration	The reported initial aquifer brine concentration has a wide degree of uncertainty, which requires a sensitivity analysis for the effect of brine concentration on CO_2 sequestration.	Section 3.2.4	[33,36, 41,42]

Effect of reactive surface area (RSA) in mineralization trapping	Most studies report the level of mineral trapping using a constant RSA. This study reports the effect of RSA on various minerals in the aquifer.	Section 3.2.5	[43–45]
Comprehensive Overview	Based on our literature review, although many studies focus on aspects of CO_2 trapping, a structured and broad overview encompassing the crucial factors governing CO_2 storage performance is lacking.	-	-

One of the key contributions and novelty of this study includes investigating the effects of capillary pressure and relative permeability hysteresis on solubility trapping and mineralization. An outline of this paper is as follows: in **Section 2,** we briefly discuss the study area, properties of the reservoir model, and geochemical considerations for this study. We follow this in **Section 3** with our results for the base case model and the effect of varying parameters that impact the interaction between fluids and rocks, aiming to identify favorable characteristics for the storage of CO_2 in deep saline aquifers. Finally, **Section 4** discusses our current state of understanding and identifies potential areas needing further investigation, and **Section 5** presents the general conclusions.

2. Characteristics of Reservoir and Geochemical Considerations

The saline aquifer model is developed with a compositional reservoir simulator (CMG-GEM, version 2023.20), which includes component transport, thermodynamic equilibrium, material balance, and phase equilibrium equations to represent the system's interaction between the brine and CO_2 [46,47]. Moreover, it accounts for the geochemical and chemical equilibrium, mineral dissolution, precipitation reactions, and changes in porosity and permeability when CO_2 is injected into a deep saline aquifer, incorporating the most critical aspects of CO_2 subsurface storage in subsurface formations. The model assumes no geomechanical effects and no impurities in primary minerals, and the impact of secondary minerals and capillary pressure hysteresis is considered negligible. We have summarized a comprehensive overview of the governing equations used in the simulator to characterize the geochemical reactions, mineral dissolution/precipitation, porosity-permeability relationship, relative permeability, and capillary pressure in **Appendix A**.

2.1. Location of the Study Area

We use the geochemical and mineral data from the upper Mt. Simon sandstone from the Illinois Basin-Decatur Project (IBDP) for the base case reservoir. The IBDP, located in Northern Illinois, is a significant demonstration site for injecting and storing CO_2 on a large scale. From 2011 to 2014, one million MT of CO_2 was injected at varying flow rates (1000-3000 MT per day) into the Mt. Simon formation [48,49]. Mt. Simon's formation is classified into three distinct sections: Lower, Middle, and Upper [50]. The Upper Mt. Simon is found in the intertidal zone and is composed of sandstone and shale deposits at a depth of 1700-1795 m and exhibits an average log porosity of 10-15% and a log permeability of 184-200 mD [51,52]. The Upper Mt. Simon sandstone is overlain by the Eau Claire formation which serves as a caprock for the interbedded sandstone, dolomitic sandstone, mudstone, dolomite, and shale that comprise the IBDP. The middle of Mt. Simon (1795 -1951 m) is characterized by poor reservoir quality with an average log porosity and permeability of 12% and 44 mD, respectively. Moreover, some regions have porosities of less than 10% [51] and permeability of less than 10 mD [11,53]. The lower sandstone shows a high average log porosity and permeability of 25% and 884 mD, respectively [51].

The base case reservoir is modeled using the properties resembling the Upper Mt. Simon sandstone, allowing us to accurately assess CO_2-fluid-rock interactions near the caprock. Furthermore, a comprehensive sensitivity analysis is presented in later sections to investigate the effect of varying operating and geophysical properties used in the base case model. It should be noted that, although the reservoir data from the Mt. Simon aquifer is used, this study does not aim to predict the performance of a specific storage site but rather provides a fundamental understanding of the impacts of various operational and geological uncertainties on CO_2 transport and sequestration in deep saline aquifers.

2.2. Reservoir Properties

An isothermal two-dimensional (2D) model with 4060 cartesian grid-blocks (divided into 203x1x20 in I, J, and K directions, respectively) is created with a top-grid depth of 1700 m, as shown in **Figure 2**. The grid block size in the I and K directions are optimized to use refined grid-blocks close to the wellbore using logarithmically spaced local grid refinement, as shown in **Table 2**.

Table 2. Reservoir grid sizing adopted in this study.

Direction considered	Number of grid-blocks	Grid sizing dimensions and additional information
I direction	203	• Dimension of central 3 grid blocks on either side of the perforation: 1.26 meters • The dimensions of the remaining 200 grid blocks are 2 to 10 meters, where grid blocks near the wellbore region are more refined. However, the blocks get coarser near the outer boundary, using logarithmic spacing between 2 and 10 m.
K direction	20	• Grid sizes are logarithmically spaced between 2 and 10 m, where grids get more refined near the wellbore region. To maintain a reservoir thickness of 100 m, the bottommost grid-block size is reduced to 1.5 m from 2 m.

The refinement scheme near the perforation zone, usually used for modeling hydraulic fractures, is required to capture the drastic change in the reservoir pressure and component saturation during the injection of CO_2 [28]. This refinement technique also improves numerical simulation convergence and reduces the simulation time needed for a compositional simulation with multiple geochemical reactions compared to the simulation model with uniform fine grids with s negligible loss in accuracy. We use a uniform grid length of 2 m in the J direction. The injection well is located in the middle of the model, and vertically perforated at the lower portion of the reservoir in the bottom three grid-blocks (I = 102, K = 18:20). Validation of the grid sizing adopted for the base case is presented in **Appendix B.1** by performing grid-sensitivity analysis.

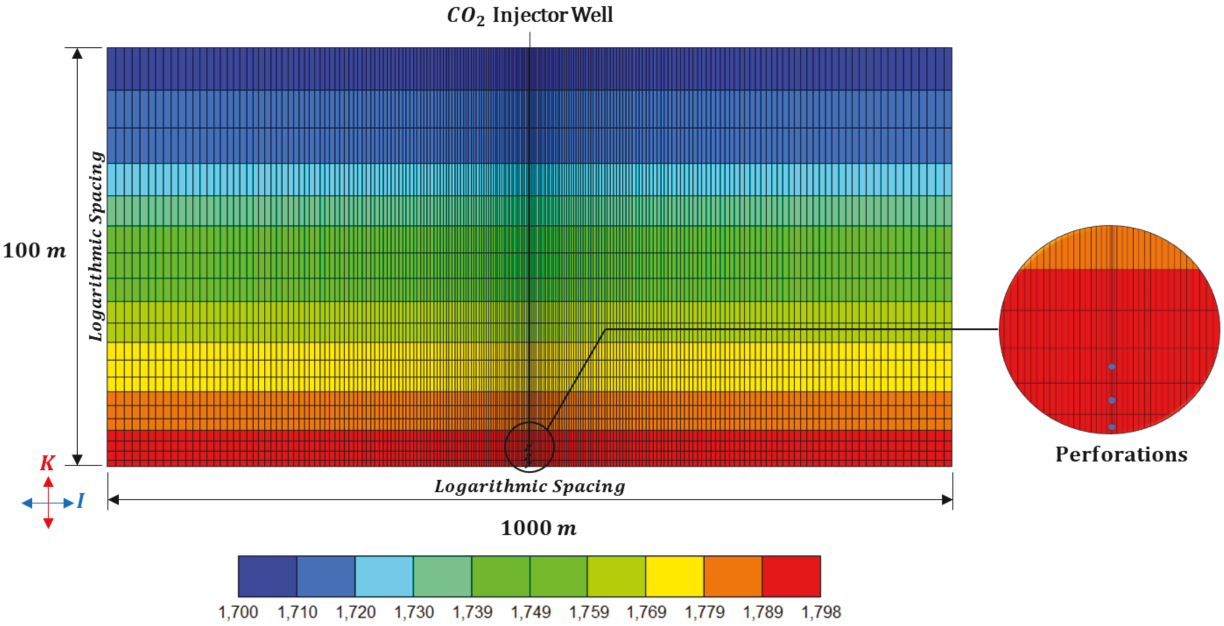

Figure 2. IK view of the reservoir. The color scale shows the depth of the reservoir from the surface. The figure is scaled by 5 in the K-direction.

We use no-flow boundaries at all four edges of the model. The top no-flow boundary represents the low permeability Eau Claire shale, which serves as a caprock. The caprock overlines the 100 m thick sandstone formation with 15% porosity and 200 mD permeability, within the range of properties reported for Upper Mt. Simon [51,52,54]. The bottom no-flow boundary represents a low permeability shale dividing the Upper and the Middle Mt. Simon formation. The aquifer's initial pressure is fixed at 17,000 KPa [40] while maintaining a constant temperature of 50°C. The water gas contact is selected as the top of the reservoir, which results in an initial condition where the reservoir is fully saturated with brine.

Pure CO_2 is injected at 100 m^3/day for ten years or until it reaches maximum bottom hole pressure (44,500 kPa). This injection rate is selected so that the maximum bottom-hole pressure constraint does not come into effect during the injection period, as we are only simulating a thin 2D section. Although volume modifiers to the reservoir boundary can be used to achieve the same effect, the leading edge of the plume needs to be carefully tracked in such models as it may artificially increase the dissolved CO_2 phase during the simulations (see **Appendix B.2**). The simulation was conducted for 1,000 years to explore the post-CO_2 injection behavior of the reservoir and analyze the fate of injected CO_2. Some important reservoir properties for the base case model are summarized in **Table 3.**

Table 3. Reservoir initial properties of the base simulation case

Parameter	Units	Value	Reference
Grid cell number	-	4,060 (203x1x20)	Current study
Length	m	1,000	Current study
Height	m	100	Current study
Depth at the top	m	1,700	[52]
Porosity	fraction	0.15	[51,52,54]

Permeability	mD	200	[51,52,54]
Pressure	Kpa	17,000	[54]
CO_2 injection rate	m^3/day	100	Current study
pH	-	5.87 [a]	[11,55]
Diffusion coefficient of CO_2 in brine	$m^2.s^{-1}$	2E-5	[17,35]

[a] Modified from Soong et al. and Zhang et al. [11,55].

2.3. Geochemical Considerations

The initial mineralogy is based on the XRD data for a core sample from the upper Mt. Simon Sandstone [51]. The XRD data in **Table 4** reveals that quartz and K-feldspar are the dominant minerals for the Mt. Simon sandstone grains. Other minerals initially present are siderite, dolomite, and calcite. The sandstone also contains plagioclase, represented by Na-endmember albite, and clay minerals, represented by kaolinite. Initially, halite is assumed to be absent in the reservoir; however, it can precipitate during the CO_2 injection process. Secondary minerals that can precipitate due to the interaction of the CO_2 with the primary minerals are not included in the study. The mineral composition can vary depending on the specific location and depth from which the sample was obtained. Researchers have reported differing mineral compositions for the upper Mt. Simon sandstone in their respective studies [51,54,56]. Even differences in sample preparation techniques can affect the results of mineral analysis and subsequently influence the reported mineral composition [57].

Table 4. List of Initial Mineral volume fractions for Mt. Simon sandstone[57].

Mineral	Chemical Composition	Mineral mass fraction (%)	Density (g/cc)	Volume fraction
Quartz	SiO_2	62	2.65	0.540
Albite	$Na(AlSi_3O_8)$	2	2.62	0.0176
K-feldspar	$KAlSi_3O_8$	22	2.56	0.198
Calcite	$CaCO_3$	1	2.71	0.00852
Dolomite	$CaMg(CO_3)_2$	3	2.84	0.0244
Kaolinite	$Al_2Si_2O_5(OH)_4$	3	2.65	0.0261
Siderite	$FeCO_3$	6	3.96	0.0350

Table 5 shows the concentrations for some of the ions in the brine solution used in this study obtained from the work of Zhang et al. [11] and Silva et al. [58]. Sodium (Na^+) and chloride (Cl^-) ions are the most dominant species in the brine, with an average reported concentration of 1.8 mols/kg of water and 9.034 mols/kg of water, respectively. The salinity is determined based on the concentration of the Na^+ ions. The concentration of H^+ ions is modified to match the initial pH of the aquifer brine reported in the literature [11,55].

Table 5. Brine chemistry used for the base case [11,58]

Ion	H^+	Ca^{2+}	Mg^{2+}	K^+	Na^+	Cl^-	Al^{3+}	Fe^{2+}
Concentration (mol/kg of H_2O)	$1.003x10^{-6}$	0.47	0.099	0.036	1.8	9.034	$1e^{-5}$	0.0014

Other significant ions include calcium (Ca^{2+}) and magnesium (Mg^{2+}). The concentrations of other ions, such as potassium (K^+), aluminum (Al^{3+}), iron (Fe^{2+}), aqueous silica (SiO_2), bicarbonate (HCO_3^-), carbonate (CO_3^{2-}), and hydroxide (OH^-) are comparatively lower, suggesting a relatively lower abundance of these ions in the brine. It should be noted that there is a wide degree of uncertainty in the reported initial aquifer brine concentration, which requires sensitivity analysis, as shown later in this study [33,36,41,42].

Geochemical reactions occur between the minerals and aqueous components (heterogeneous reaction) and among the components within the aqueous phase (homogeneous reaction) (refer to **Appendix A.2.** for the equations used to define geochemical reactions in the simulator). Although other equilibrium reactions may be applicable, we only consider the following in our simulation.

$$H_2O = OH^- + H^+ \tag{1}$$

$$H_2O + CO_2 = HCO_3^- + H^+ \tag{2}$$

$$CO_3^{2-} + H^+ = HCO_3^- \tag{3}$$

Table 6 shows the reactions and kinetic parameters used in this study for mineral dissolution/precipitation (refer to **Appendix A.3.** for detailed information). Although different log-rate constants are reported in the literature depending on the underlying reaction mechanisms, we use values reported for the acid mechanism whenever available. There is also a wide variation in the reported reactive surface area, which will be analyzed extensively in Section 3.2.5.

Table 6. Mineral dissolution/precipitation reactions and kinetic parameters.

Reaction	Log-rate constant, $\log k_b$, $[mol/(m^2 s)]$ at 25^0C	Reactive surface area, $\widehat{A}_J$, $[m^2/m^3]$	Activation energy, $E_{\alpha\beta}$, $[j/mol]$	Ref.
$Quartz\ (SiO_2) = SiO_{2(aq)}$	-13.4	2,650	90,900	[59]
$\mathrm{K-feldspar\ (KAlSi_3O_8)} + 4\,H^+ = 3\,SiO_2 + Al^{3+} + K^+ + 2\,H_2O$	-10.06	995,840	51,700	[21, 59]
$Albite\ (NaAlSi_3O_8) + 4\,H^+ = 3\,SiO_2 + Al^{3+} + Na^+ + 2\,H_2O$	-10.16	1,021,800	16,600	[11]
$Calcite\ (CaCO_3) + H^+ = HCO_3^- + Ca^{2+}$	-0.3	2,710,000	14,400	[11, 59]
$Dolomite\ (CaMg(CO_3)_2) + 2\,H^+ = 2\,HCO_3^- + Mg^{2+} + Ca^{2+}$	-3.19	284,000	56,700	[11, 59]
$Siderite\ (FeCO_3) + H^+ = HCO_3^- + Fe^{2+}$	-10.097	3,880.8	56,000	[60]

$Kaolinit\ (Al_2Si_2O_5(OH)_4) + 6\ H^+ = 2\ SiO_2 + 2\ Al^{3+} + 5\ H_2O$	-11.31	1,014,950	65,900	[21, 59]
$Halite\ (Nacl) = Cl^- + Na^+$	-5.00	176	200	[47]

Accounting for the effects of capillary pressure, relative permeability, and hysteresis modeling are crucial in reservoir simulation. The relative permeability curves for water and gas were generated using the Brooks-Corey function [61] based on the experimental data for the Mt. Simon aquifer [53]. As the aquifer is water-wet, the liquid phase relative permeability curves are assumed not to vary for drainage and imbibition processes [32,62]. However, the gas phase relative permeability varies depending on whether it displaces the liquid or is displaced by it. This hysteresis in relative permeability is modeled by Land's approach [63]. The Brooks-Corey equation [61] is used to obtain the capillary pressure for drainage based on the experimental data by Krevor et al. [53]. **Figure 3** shows the relative permeability with some of the scanning curves for K_{rg} and the capillary pressure curve used in the base case model. The capillary pressure hysteresis was not considered here as prior studies have shown that it has negligible impact on CO_2 trapping by different mechanisms but adversely affects the simulation time [9,32]. The relevant correlations and experimentally determined parameters for Mt. Simon sandstone [53] used for generating the curves in **Figure 3** are presented in **Appendix A.4**.

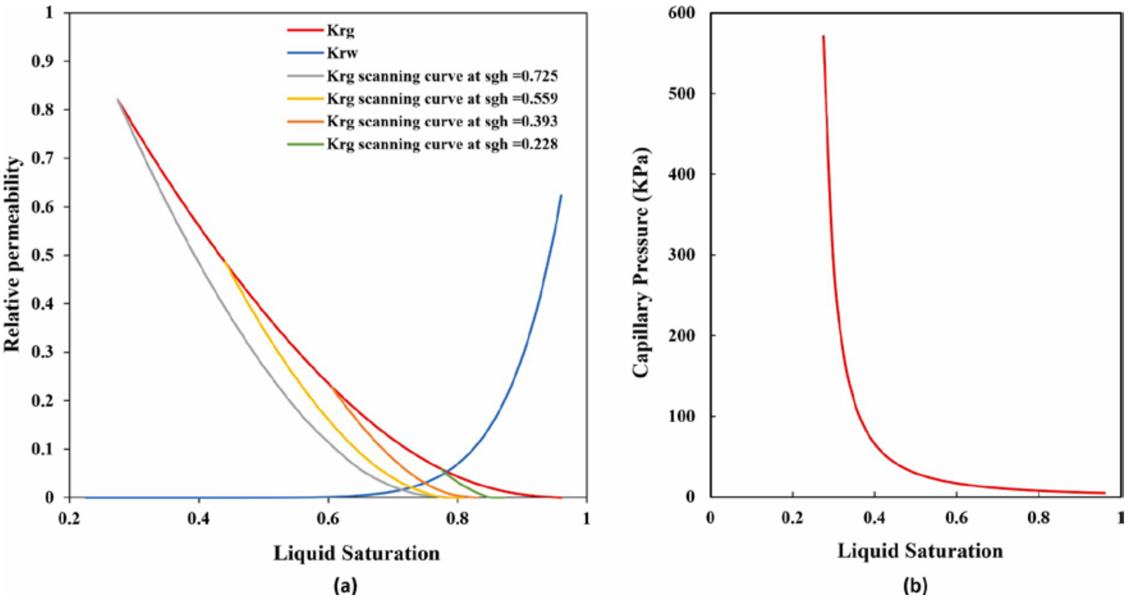

Figure 3. (a) Relative permeability and scanning curve for drainage and imbibition and (b) Capillary pressure curve.

3. Results

3.1 Base Case

This section evaluates the changes in CO_2 flow and storage behavior of the reservoir in the base case model, described in **Section 2**. The base case simulates a 1000-year process with ten years of active injection followed by the monitoring phase and calculating the amount of CO_2 stored by different trapping mechanisms. The impact of relative permeability hysteresis and capillary pressure are evaluated using additional simulations. Furthermore, grid-sensitivity is performed to validate the accuracy of the base case model using a model with more refined grid-blocks (**Appendix B**).

3.1.1 CO_2 Storage by Different Mechanisms

Figure 4 shows the fraction of CO_2 stored by different trapping mechanisms for the base case simulation over the 1000 years. Initially, there is an instantaneous increase in the fraction of dissolved CO_2 as the injected supercritical gas comes in direct contact with the aquifer brine. However, as the local equilibrium is established between the supercritical CO_2 phase and the brine, the rate of CO_2 dissolution cannot keep up with the injection rate, and the fraction of the supercritical phase increases rapidly. After 33 days, the fraction of the supercritical phase (~50.5%) exceeds the dissolved phase (~49.5%) and keeps on increasing till the end of the injection period (10 years). Moreover, after nine months of injection, when the CO_2 reaches the reservoir's upper layer, the upward path is already saturated with dissolved CO_2. As a result, the fraction of mobile CO_2 continues to increase steadily after the nine months of the CO_2 injection. **Figure 4c** shows at the end of 10 years, 84.0% of the injected CO_2 exists in the supercritical phase. Of the 84.0% $ScCO_2$, 14.8% exists as a residually trapped and 69.2% in the mobile phase. The remaining CO_2 is dissolved (15.4%) and mineralized (0.55%). After the injection stops, shown in **Figure 4b**, we observe a sharp inflection in the fraction of residually trapped $ScCO_2$, which results in a significant drop in the fraction of mobile CO_2 in the reservoir. This reduction in mobile CO_2 is due to the relative permeability hysteresis and capillary forces, which will dominate when the injection stops. The brine displaced during the injection will push out the supercritical phase from the pore spaces, leaving behind a trail of disconnected ganglia of $ScCO_2$, which will stay trapped within the pores.

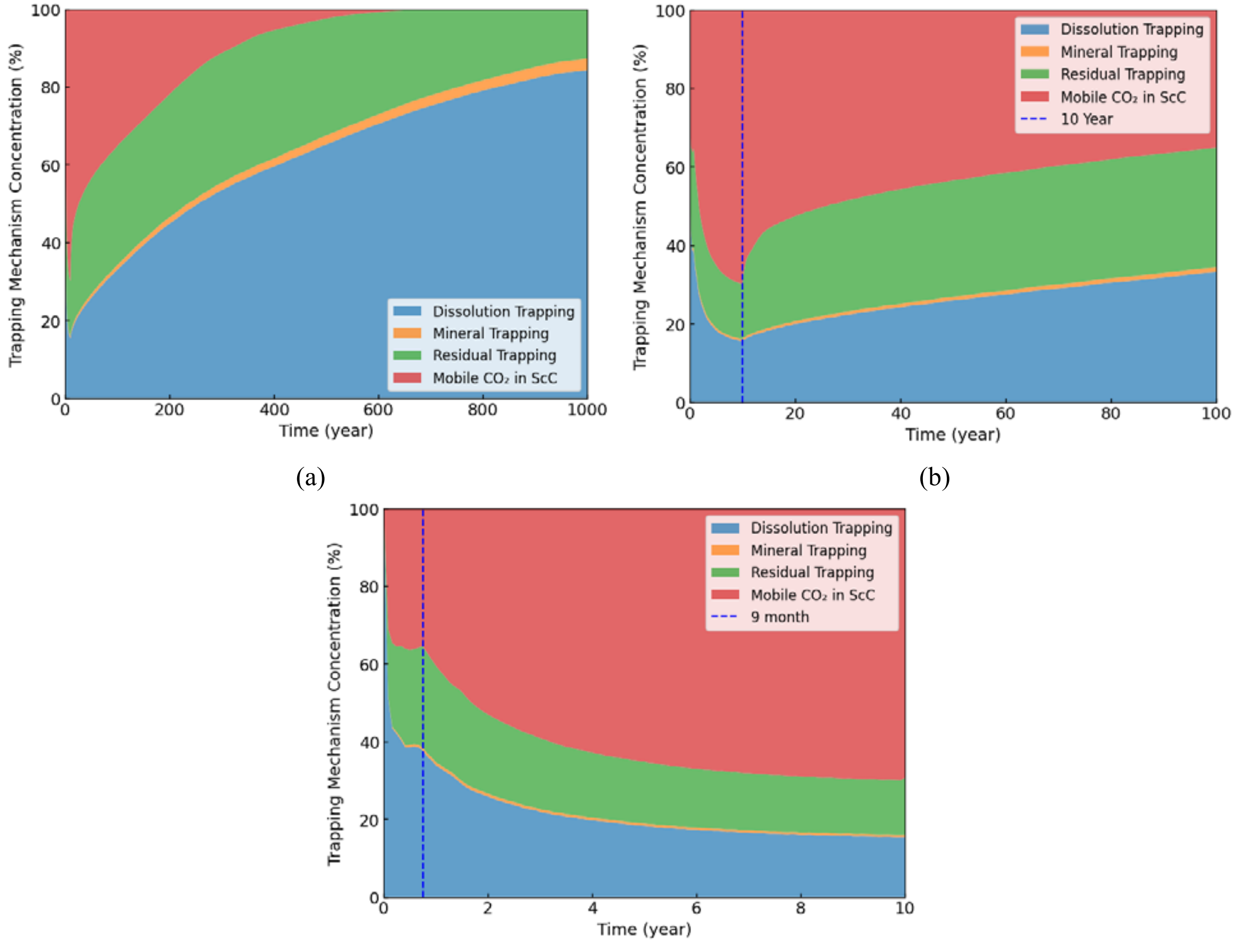

(a)

(b)

(c)

ScC: Supercritical Condition

Figure 4. Contribution of different CO_2 trapping mechanisms: (a) 1000 years, (b) magnified view up to 100 years, (c) magnified view up to 10 years.

Although the fraction of dissolved and the residually trapped phases are almost in parity (15.4% vs 14.8%) after 10 years, the fraction of residually trapped CO_2 increases rapidly for the next 12 years. After around 15 years from the start of the simulation, there is a maximum difference of 7.20% between the fraction of CO_2 in the dissolved and the trapped phase. After this time, the increase in residual trapping slows down and reaches the maximum value of 33.5% after around 359 years of simulation. About 80 years after the beginning of the simulation, the fraction of CO_2 sequestered by dissolution trapping becomes higher again than the residual trapping (30.3%). The fraction of mobile CO_2 decreases rapidly throughout this period, contributing to all the other trapping mechanisms. The most significant increase is observed in dissolution trapping, which is highly enhanced by Rayleigh-Taylor instability of the dissolved CO_2 at different continuous vertical reservoir layers. The CO_2-rich dense brine at the top of the reservoir descends, and the buoyant bottom layer rises, continuously reducing the mobile phase CO_2 close to the caprock and residually trapped CO_2. We observe almost complete dissolution of the mobile CO_2 (< 0.1% remaining) after 684 years, and the only supercritical phase in the aquifer is residually trapped. **Figure 4c** shows hardly any CO_2 sequestered by mineralization for the first ten years of injection (0.55%). Among these mineralized components, calcite contributes the majority at 78.46%, whereas dolomite and siderite contribute 21.26% and 0.28%, respectively. This value (0.55% mineralization) does not account for the dissolution or precipitation of minerals that do not contribute to the sequestration of CO_2 (such as halite and non-carbonate minerals). At the end of 1000 years, around 2.97% of total injected CO_2 is sequestered in the form of solid precipitates, where most of them mineralized as calcite (78.33%), and the rest of them sequestrated as dolomite (21.36%) and siderite (0.31%).

3.1.2 pH Evolution with Time

Initially, the aquifer brine has a pH of 5.87, similar to the values reported in the literature [11,55]. After injection, the CO_2 dissolves in the brine, forming a weak acid, which reduces the pH along the path of CO_2 flow. **Figure 5b** shows that after the injection period, the pH near the well bore rapidly drops from 5.87 to 4.45, gradually reducing to 4.13 after 10 years of simulation. The pH change is only seen close to the wellbore for the injection layer, and no pH change is observed beyond 100 m (**Figure 5b**). However, **Figure 5a** also shows that the pH change in the upper region of the reservoir extends to over 700 m as the injected CO_2 rises to the top of the aquifer due to buoyancy. For later times, the pH of lower regions (towards the injection layer) also drops as the dissolved CO_2 migrates towards the bottom of the aquifer. The porosity and permeability change due to CO_2 interacting with reservoir rock and brine is limited to the regions with a pH change (see **Fig. 12**).

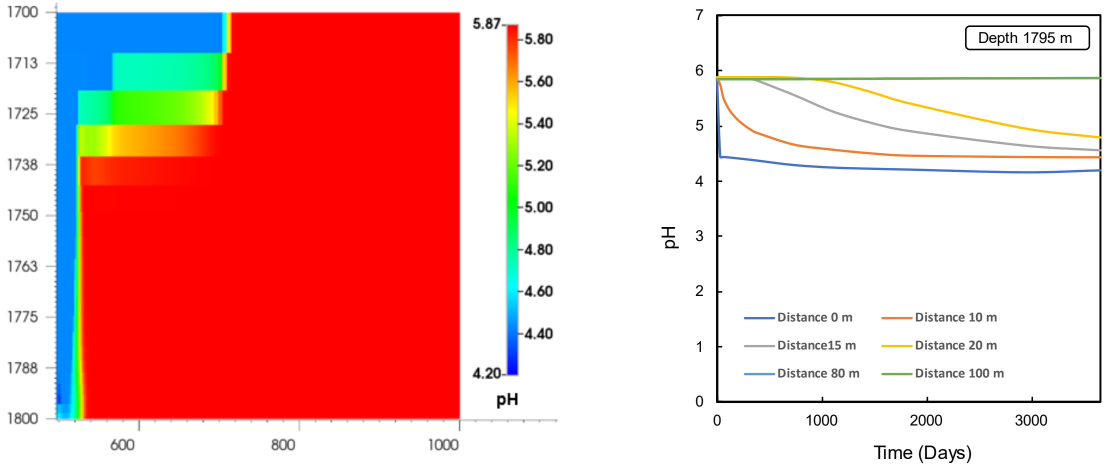

(a) (b)

Figure 5. pH distribution inside the reservoir after 10 years of CO_2 injection, (b) changes in pH with respect to time for different distances from the wellbore at a depth of 1795 m (injection layer) after 10 years.

3.1.3 Effect of Relative Permeability Hysteresis and Capillary Trapping

As CO_2 is injected into a saline aquifer, the drainage relative permeability curves control the flow behavior in grid blocks where the $ScCO_2$ (non-wetting phase) saturation increases. When the saturation of the $ScCO_2$ decreases due to its migration to other blocks or its displacement by the brine, imbibition relative permeability curves determine the saturation-dependent permeability [64]. This difference in relative permeability results in the higher critical gas saturation needed for the non-wetting fluid to flow out from the porous media, resulting in a trapped phase [32]. Similarly, capillary pressure (the difference between the pressure due to the non-wetting and wetting phase) results in a trapped non-wetting phase inside the pore spaces. Although the short-term impact of capillary pressure and relative permeability hysteresis is apparent for residual trapping mechanisms, its long-term impact on solubility trapping and mineral trapping is unclear. To investigate this impact, we run three additional cases (**Table 7**) and compare the results with the base case. For **case 1**, we exclude both the relative permeability hysteresis and the capillary pressure from the simulation. For **cases 2 and 3**, we exclude relative permeability hysteresis but include capillary pressure and vice versa to isolate their impact on different trapping mechanisms during the simulation period.

Table 7. Summary of the simulation runs for relative permeability and capillary pressure

Case	Hysteresis (K_r)	Capillary (P_c)
Base	Yes	Yes
1	No	No
2	No	Yes
3	Yes	No

Figure 6 shows the evolution of the percentage of injected CO_2 sequestered by different trapping mechanisms over 1000 years of simulation. For cases 1-3, including the base case, the reservoir does not reach the maximum bottom hole constraint imposed on the wells; hence, the total $ScCO_2$ injected is the same for all cases. At the end of the first month (31 days), base case and case 2 show similar amounts of CO_2 trapped by different mechanisms and CO_2 in the mobile phase. As the mineralization reactions are kinetically unfavorable during earlier times, only a small proportion (~0.3%) of CO_2 mineralization is observed for all the cases. We observe larger mineralization for case 3 for the first 60 days, after which the base case and case 2 will have a higher fraction of CO_2 mineralized. After 1000 years of simulation, the maximum mineralization is in the following order: case 2 (3.36%), base case (2.97%), case 1 (1.38 %), and case 3 (1.60%). From this result, capillary pressure has the most significant impact on CO_2 sequestration by mineralization. If capillary pressure is ignored (cases 1 and 3), the sequestration by mineralization is significantly lower compared to cases where capillary pressure is considered. The inclusion of capillary pressure in the base case and case 2 results in higher mineralization as a significant fraction of the $ScCO_2$ becomes occluded in pores due to capillary pressure rather than being displaced as a continuous plume. These occluded $ScCO_2$ are dispersed in numerous pores, increasing the contact area and concentration gradient between different species in the various phases, leading to higher mineralization than in cases with no capillary forces[65].

Similar results are observed for dissolution trapping, where the inclusion of capillary pressure significantly improves CO_2 dissolution after various periods. After ten years (injection period), where capillary pressure is active for the base case and case 2, around 15.5% of the injected CO_2 dissolves compared to around 11.15% for cases 1 and 3. This trend continues during the monitoring phase, where the fraction of injected CO_2 in the dissolved phase is significantly higher in the base case and case 2. Moreover, the mobile CO_2, which can leak from primary or induced fractures, is significantly lower in the base case as a significant fraction of CO_2 is trapped due to the residual trapping. For example, as shown in **Figure 6**, after 500 years, the base case has a significantly lower fraction of the mobile CO_2 (2.51%) than case 2 (15.99%), where capillary pressure is present but not the relative permeability hysteresis. However, mobile CO_2 for cases 1 (62.8%) and 3 (55.91%) are much higher simultaneously. This trend is also seen for other intermediate periods. After 1000 years of simulation, the base case and case 2 exhibit the most effective

CO_2 immobilization through secure trapping mechanisms. On the contrary, cases 1 and 3, which do not include capillary pressure, have a significant fraction of mobile CO_2 at ~52% and ~45%, respectively. The rate of dissolution and the transport of dissolved CO_2 is governed by the pore-scale configuration of different phases, which is controlled by the capillary pressure [66,67]. Hence, including capillary pressure significantly improves dissolution-trapping, resulting in a low fraction of mobile $ScCO_2$.

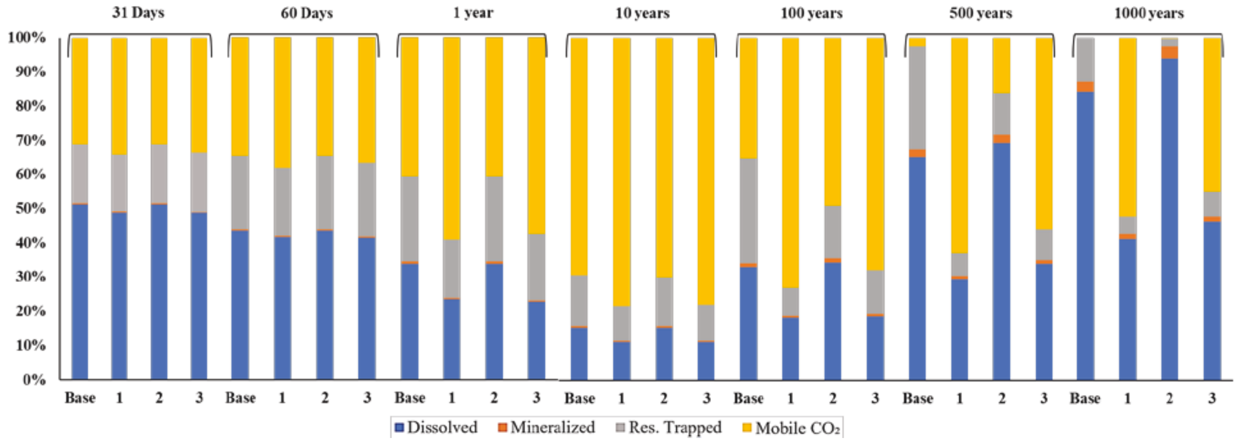

Figure 6. The percentage of CO_2 sequestered by different mechanisms in the first 31 days, 60 days, 1 year,10 years, 100 years, 500 years, and 1000 years.

The results shown in **Figure 6** were further verified by analyzing the gas saturation in the grid blocks after 50 years of simulation. As shown in **Figure 7**, the mobile phase CO_2 is highly concentrated around the top central grid blocks for cases 1 and 3, which can be attributed to the exclusion of capillary pressure in these models. This is also evident from the maximum gas saturation of 0.51 for cases 1 and 3, whereas base case and case 2 have a maximum gas saturation of 0.28. Other periods show similar results, and the results for 50 years are presented here to highlight the differences among the studied cases.

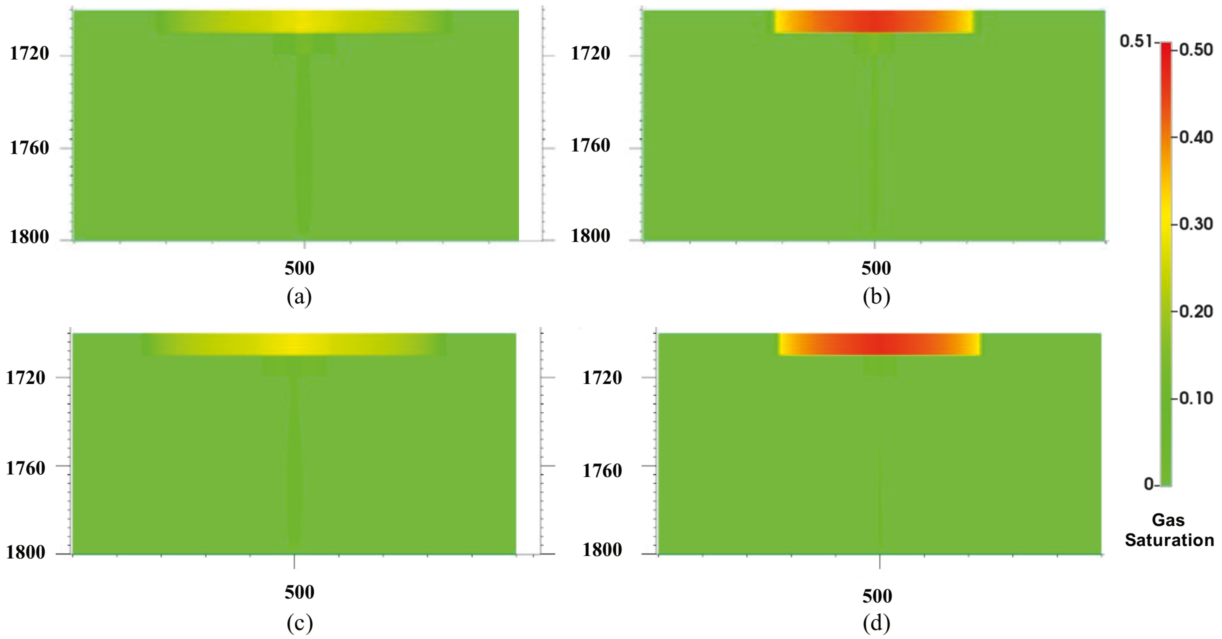

(a) (b) (c) (d)

Figure 7. Gas saturation after 50 years of simulation for (a) Base Case, (b) Case 1, (c) Case 2, (d) Case 3.

These findings emphasize the significance of capillary pressure and relative permeability hysteresis when predicting the fate of injected CO_2. The capillary pressure and relative permeability hysteresis promote the sequestration of the injected CO_2 using mechanisms that limit mobility and prevent potential leakage through undetected or reactivated fractures.

3.1.4 Mineralization Behavior and Impact on Flow Properties

Although the fraction of CO_2 trapped by mineralization is relatively small compared to other mechanisms (**Figure 4**), precipitation and dissolution reactions may still significantly impact the reservoir's flow properties. Furthermore, the CO_2 sequestered by mineralization (**Figure 4**) only considers carbonates (calcite, dolomite, and siderite) and does not include other non-carbonate minerals. Although the dissolution and precipitation of other non-carbonate minerals do not contribute to CO_2 mineralization, they will still alter the reservoir flow properties. **Figure 8a** shows the precipitation and dissolution behavior of all the minerals simulated in the base case after 1000 years. Calcite and dolomite are the two minerals that contribute to the formation of carbonate precipitates. Siderite shows negligible precipitation during the simulation period. Other minerals that do not contribute to CO_2 mineralization, such as halite, quartz, and kaolinite, precipitate or dissolve during the simulation period. Although the long-term behavior shows stable precipitation or dissolution, a close inspection reveals a complex behavior for the considered minerals. The injection of CO_2 into the formation leads to its dissolution and subsequent reaction with the formation fluid, resulting in the production of H^+ , carbonate (CO_3^{2-}), and bicarbonate ions (HCO_3^-) ions. These fast aqueous reactions **(Eq. 1-3)** decrease the pH locally from 5.87 to 4.2. This acidic environment facilitates reactions with ions such as Ca^+, Mg^{2+}, and Fe^+ and minerals in the rock matrix, resulting in carbonate minerals' dissolution and precipitation. Calcite, dolomite, and siderite are observed to start to precipitate from the beginning, as shown in **Figure 8b**. However, the precipitation reaction of calcite is significantly faster than dolomite or siderite. After calcite, halite shows the most rapid precipitation during the first year of injection. We also observe that the feldspar group (albite and k-feldspar) starts to dissolve in the initial simulation period, which slows down as the simulation progresses, as presented in **Figure 8b**. After 1000 years, kaolinite is the only mineral that dissolves with other minerals precipitating due to their reactions with the injected CO_2 and brine. The H^+ ions from the precipitation of reactions result in the dissolution of kaolinite. The aqueous silica obtained from kaolinite dissolution helps precipitate the feldspar minerals and quartz.

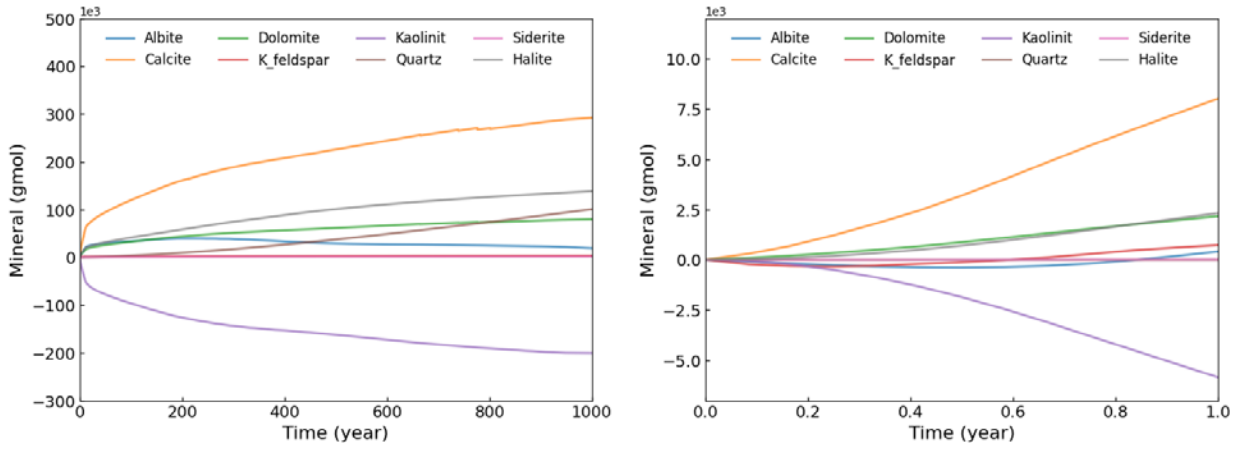

(a) (b)

Figure 8. (a) Mineral concentration change (gmol) for the base case simulation for 1000 years (b) Same as a but for only year one.

Next, we evaluate the change in porosity and permeability due to the reactive dissolution of minerals and precipitation of injected CO_2. A grid block in the perforated region is selected, and the porosity and permeability change are evaluated using **Eq. A.14 to A.16**. Furthermore, the corresponding permeability change is calculated using the K-C relationship (**Eq. A.16**) with an exponent (ξ) of 3. **Fig. 9** shows the change in porosity and permeability of the perforated grid block (102, 1, 18). Also, halite precipitation is superimposed on **Figure 9** to illustrate a clear relationship between halite precipitation and porosity/permeability reduction. At the end of 10 years (injection period), the porosity decreases from 0.150 to 0.133, an 11.6% reduction from the initial value. The resulting reduction in permeability, calculated from K-C at the end of 10 years, is 131 mD, a 34.2% reduction compared to the initial reservoir permeability. The significant permeability/porosity change can be attributed to the large halite precipitation, which was significantly higher than the other minerals for the grid block shown in **Figure 9**. However, this effect is only observed in the grid block with perforations. We observe negligible halite precipitation in other grid blocks away from the perforations, as shown in **Appendix C.2 (Fig. 29e)**.

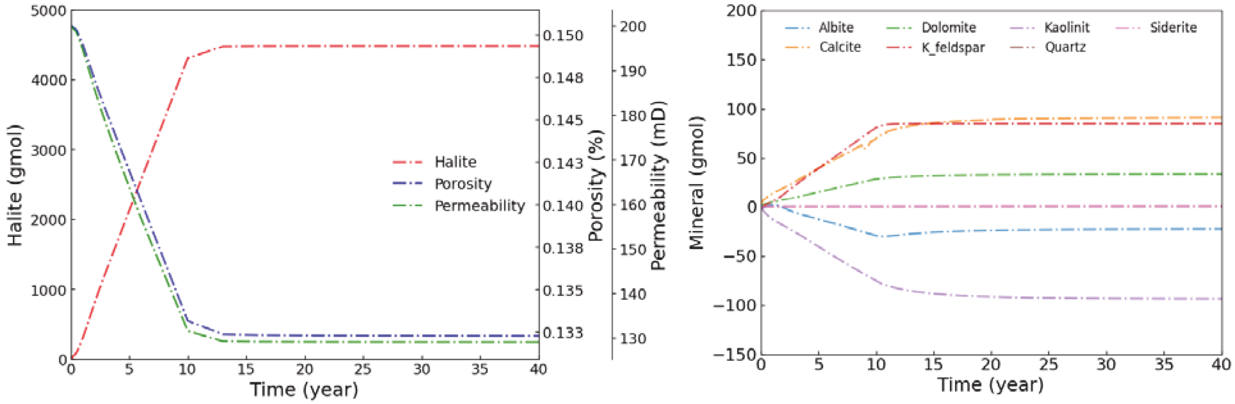

(a)

(b)

Figure 9. Mineral concentration change (gmol) and porosity and permeability change near the injection well.

During the injection into an aquifer, three distinct zones are created with the injection of CO_2 in the reservoir: dry out, two-phase zone, and wetting phase saturated zone (**Figure 1**). The water starts to evaporate, and the concentration of the salt increases because of the flooding front of the CO_2 toward the aquifer. When the salt concentration exceeds the solubility threshold, it precipitates. This is why large halite precipitation close to top perforation will experience the most significant vaporization of water within the reservoir. The amount of salt precipitation is higher when the capillary pressure is considered in the simulation. The reason behind this is capillary-driven backflow, which supplies brine for the two-phase zone, as shown by a larger water saturation value around the injection zone when capillary pressure is considered in **Figure 10a** compared to the one without any capillary pressure, shown in **Figure 10b**. When the capillary pressure surpasses the pressure gradient caused by the injection fluid (CO_2), water moves backward to the two-phase zone. Consequently, vaporization occurs, leading to the formation of halite.

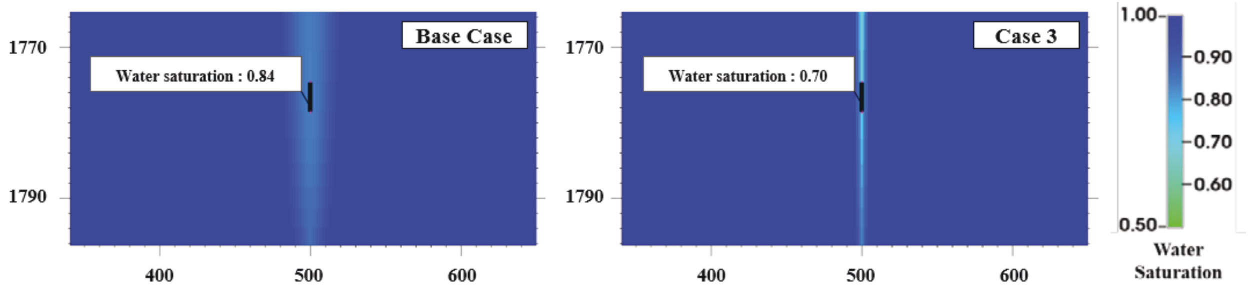

(a)

(b)

Figure 10. Water saturation around the injection zone for a) the capillary pressure and relative permeability hysteresis are considered and b) only relative permeability hysteresis is considered. The highlighted grid block (black) shows the water saturation value for each after 10 years of simulation.

Although there is high precipitation around the wellbore, throughout the other reservoir regions, we observe that the porosity and permeability increase over the simulation period. The porosity of the top layer, which is assumed to be a caprock, was analyzed by selecting several grid blocks at varying distances for the entire simulation period.

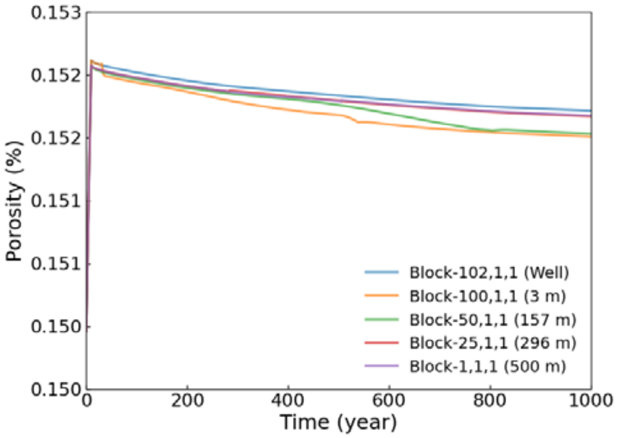

Figure 11. The change in porosity of the topmost layer over the period of 1000 years.

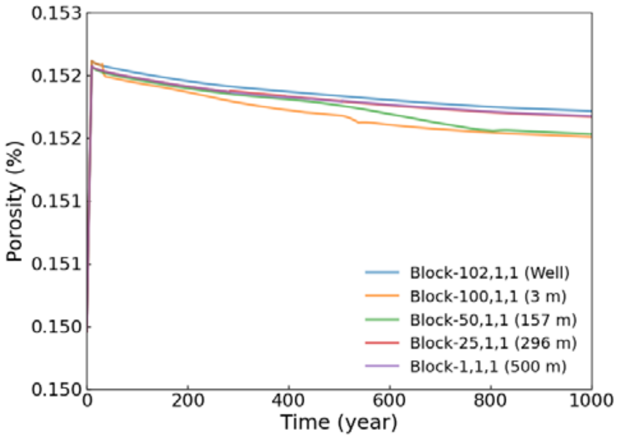

Figure 11 shows that for all the distances analyzed, although the porosity increases to a maximum value at 10 years, it slowly declines throughout the simulation period for all the grid blocks. Furthermore, as seen in **Fig. 12,** we observed an increase in the porosity all over the reservoir, except near the injection point, throughout the simulation period, which agrees with other studies [68,69]. The maximum porosity of 0.1527 (~1.5% increase from the base case) is observed at 10 years. The relative significance of kaolinite dissolution compared to the precipitation of other minerals leads to an overall increase in the porosity of the reservoir. The increase in porosity due to the dissolution of minerals leads to a slight increase in permeability throughout the reservoir except for the region near the wellbore. Furthermore, this flow property change close to caprock may increase the risk of CO_2 leakage in case of a substantial increase in porosity and permeability. However, the current study does not distinguish the mineralogical makeup of the caprock and the storage zone, which is significantly different [70] and will be evaluated in future studies. The simulation here also does not consider secondary minerals that can precipitate; however, the results presented here show the complex precipitation and dissolution behavior of primary minerals during the injection of CO_2 in deep saline aquifers.

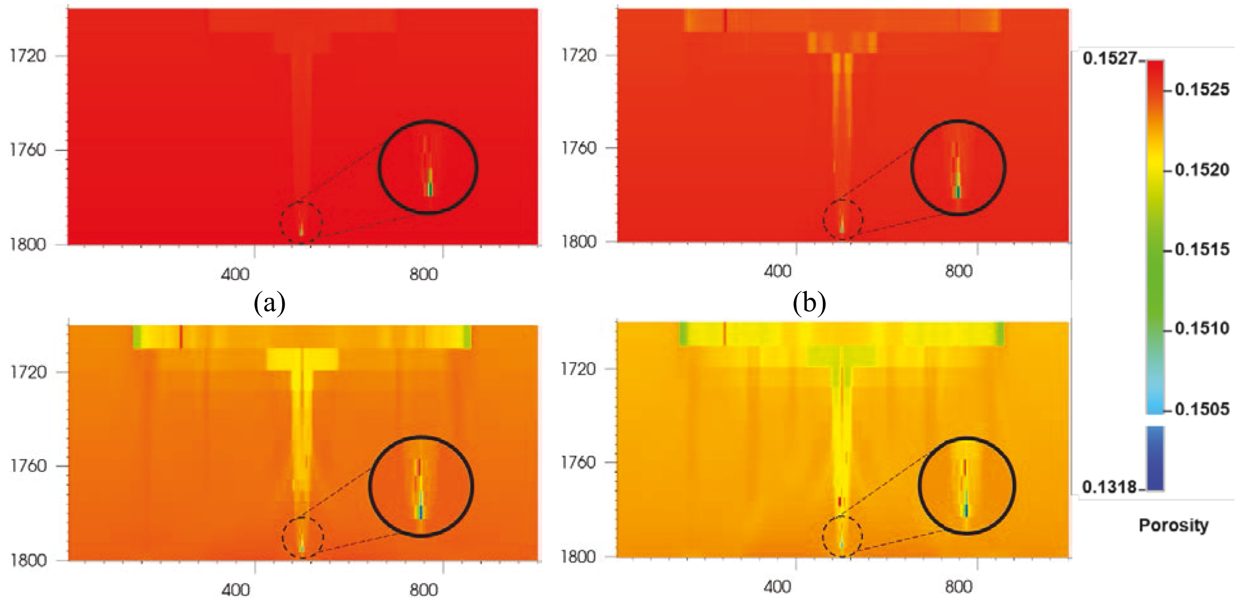

(a) (b)

(c) (d)

Effective porosity near the injection zone is magnified for enhanced visualization

Figure 12. Effective porosity for the base case model after (a) 10 years, (b) 100 years, (c) 500 years, and (d) 1000 years. The near-well bore region (dotted circle) is zoomed (solid circle) in the figure for better clarity.

3.2 Effect of Different Parameters in the Sequestration Process

In this section, we undertake a sensitivity analysis to quantify the influence of critical parameters on fluid-rock interaction and the sequestration process. Additional 37 simulations were performed, covering a wide range of critical parameters to analyze their impact. A complete description of the properties of the simulation cases is provided in **Table 8**. Although the selected parameters may interact with each other, we vary each of them individually to isolate their impact on key indicators evaluated in this study. The interaction effects among several parameters, which require additional simulations, will be considered in future studies.

Table 8. Critical parameters and the reasons to pick them for the sensitivity analysis.

Parameter	Reason for parameter selection	Values	Cases
Injection rate	A decision parameter that can be optimized for maximum storage security. The base	50 m^3/day for 20 years, 100 m^3/day for 10 years	5, Base, and 6

	case CO_2 injected volume is maintained for all the runs.	*, and 200 m^3/day for 5 years.	
Permeability	An uncertain parameter that determines the flow capacity of a reservoir. The range reported for Mt. Simon sandstone reservoir is ~10-884 mD.	7.5 mD, 200 mD * and 900 mD	7, Base, and 8.
Porosity	An uncertain parameter that determines the storage capacity of an aquifer. The range reported for Mt. Simon sandstone reservoir is ~10-25 %.	8%, 15%*, and 25%.	9, Base, and 10
Salt concentrations	An uncertain parameter that determines the rock-brine-CO_2 interactions and affects the mineralization. Range reported for different formations used.	Changed individual salt concentration from low to high.	Base, 11-20
Reactive surface area	An uncertain parameter that determines the rock-brine-CO_2 interactions and affects the mineralization. This study analyzed the range reported in different literature.	Changed individual mineral reactive surface area from low to high.	Base, 21-41

* Denotes the values for the base case model.

3.2.1 Effects of Injection Rate

The injection rate is one of the most important decision parameters during a CO_2 sequestration project. Although high injection rates allow for rapid storage, it can also lead to high reservoir pressure buildup, which may negatively affect the storage security of the injected gas. We compare the base case model with cases 5 and 6 by injecting an equal volume of CO_2 at different injection rates and periods. Cases 5 and 6 use the injection rate of 50 m^3/day for 20 years and 200 m^3/day for CO_2 for 5 years, respectively.

CO_2 trapping in different mechanisms for cases 5, 6, and the base are compared in **Figure 13**, which shows that the faster injection rate (case 6) leads to higher dissolution, mineralization, and residual trapping over 100 years compared to the cases with lower injection rate (case 5 and base case). For the case with a higher injection rate, a larger volume of CO_2 encounters the in-situ brine, resulting in a larger cumulative concentration gradient. This process leads to enhanced dissolution and mineralization trapping. For higher injection cases, the relative permeability hysteresis and capillary pressure also become dominant sooner as the injection lasts for shorter periods. This early onset of relative permeability hysteresis and capillary pressure leads to higher residual trapping for higher injection cases in **Figure 13c.** Spiteri and Juanes [71] also reported a similar result in their study.

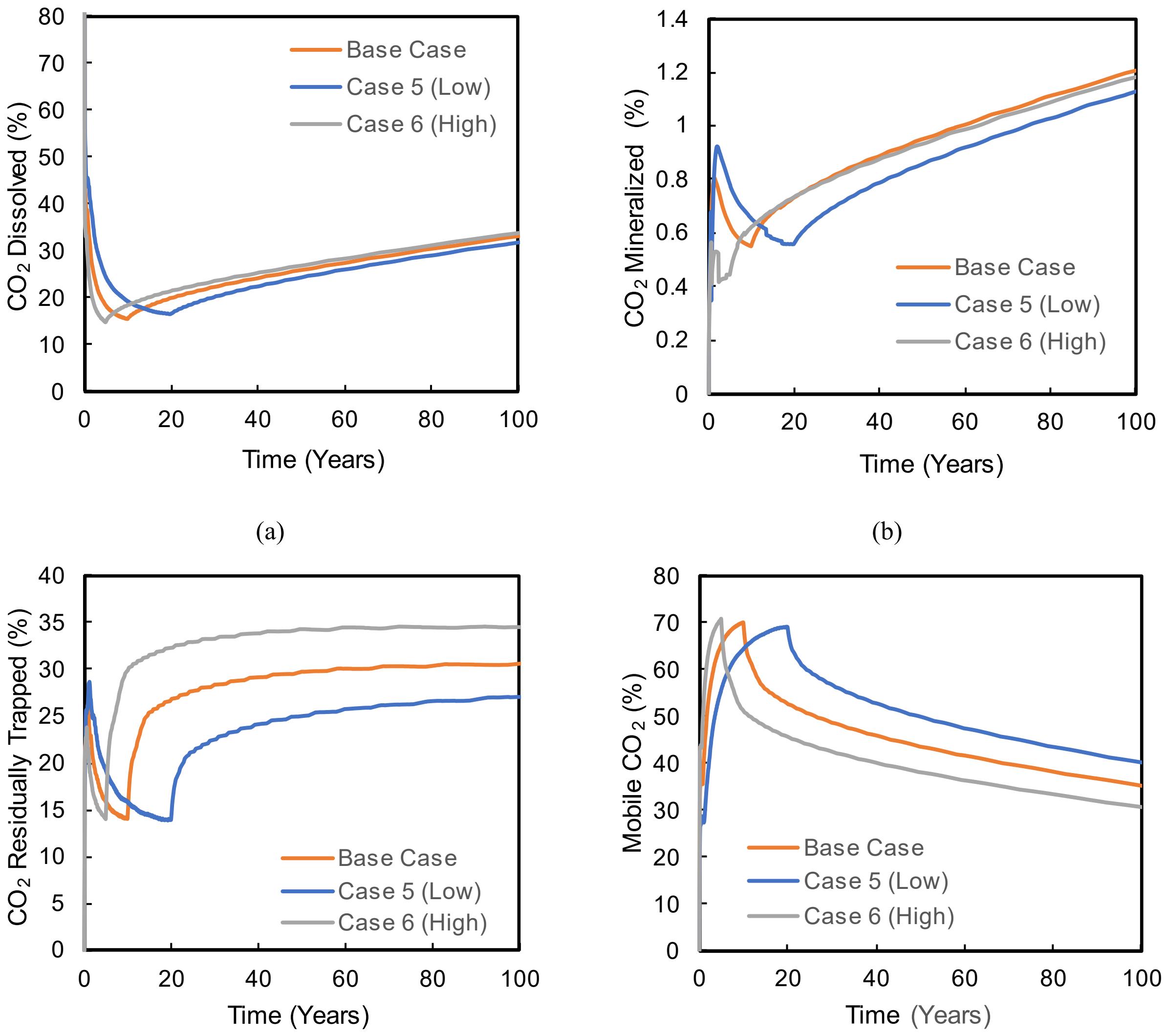

(a) (b)

(c) (d)

Figure 13. Effect of injection rate in CO_2 trapping by dissolution, mineralization, residual, and mobile CO_2 (a), (b), (c), and (d) after 100 years of simulation.

However, over the 1000 years, case 5 (lower injection rate) shows a slightly higher CO_2 dissolution and mineralization compared to case 6 and base case in **Figure 14.** The primary reason behind this dominance can be attributed to enhanced convective mixing due to the Rayleigh Taylor instability in the lower injection case. During the initial injection period, a significant volume of CO_2 moves to the top of the aquifer instead of being residually trapped or dissolved in the lower zones for a low injection case. As the top layer dissolves in brine, it becomes heavier than the subsequent layer below. This density gradient across each layer results in convective mixing, significantly enhancing the dissolution of CO_2 [7]. The topmost layer for the low injection case shows higher gas saturation compared to the other cases which is highlighted by **Fig. 26 (Appendix C.1)**, which shows the gas saturation plot for all three cases. Prior studies have also shown that convective mixing is slow initially but can significantly enhance the dissolution when the cyclic process fully develops [5,7,72].

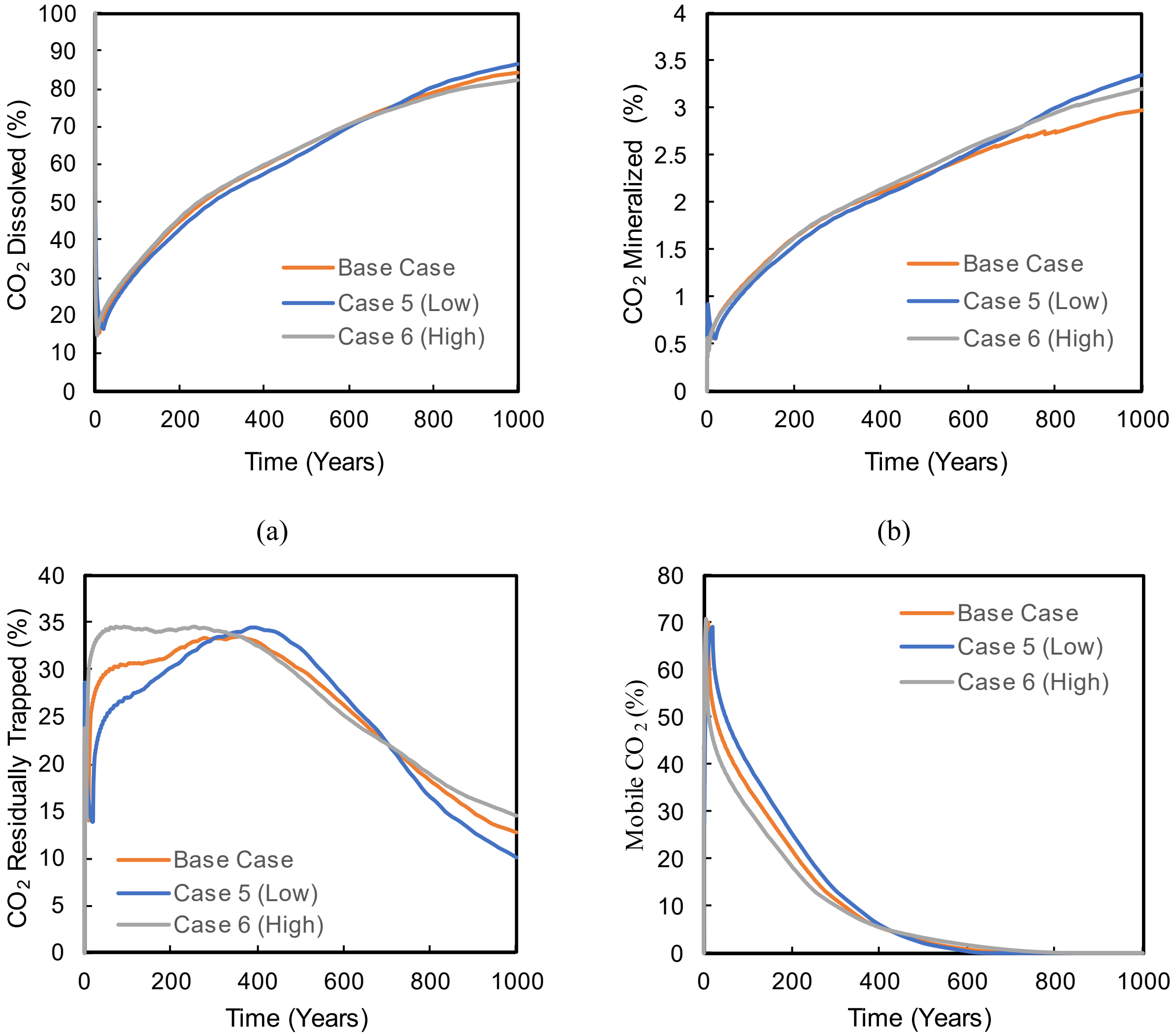

(a) (b)

(c) (d)

Figure 14. Effect of injection rate in CO_2 trapping by dissolution, mineralization, residual, and mobile CO_2 (a), (b), (c), and (d) after 1000 years of simulation.

Although the slower injection rate case results in the highest percentage of CO_2 dissolved throughout the simulation compared to the others, it may not be suitable for the sequestration project for two reasons. The first reason is the high gas saturation persists close to the caprock for the case with a low injection rate (**Appendix C.1, Fig. 26a).** This increases the risk of CO_2 leakage to the atmosphere in the case of fracture reactivation due to the interaction with CO_2. The second reason is slow injection reduces the NPV of the project, which makes it economically unattractive compared to a higher injection case [73]. A faster injection rate will lead to faster accumulation of carbon credits and other incentives with potentially lower operating costs [40].

3.2.2 Effects of Permeability

Permeability is one of the most important flow properties determining fluid transport in porous media. It is also one of the most uncertain parameters, varying significantly depending on the reservoir region. For example, the permeability of the Mt. Simon aquifer varies between 7.5 mD and 884 mD depending on the zone in the aquifer [51]. In addition to the base case model with a permeability of 200 mD, we evaluated two other permeability cases of 7.5 mD to 900 mD to cover a wide range of possible values for permeability.

Overall, it is observed that higher permeability leads to increased dissolution and mineralization of injected CO_2, which is supported by the reduction in the residually trapped and mobile CO_2 **(Fig. 15a-d)**. In the base case model, less than 1% mobile CO_2 remains after ~600 years of simulation CO_2 **(Fig. 15d)**. In the higher permeability scenario, CO_2 migrates more rapidly toward the upper layer in a shorter time frame and spreads laterally beneath the caprock layer. This extensive migration exposes the CO_2 to a larger volume of fresh formation fluid, resulting in enhanced dissolution and mineralization processes.

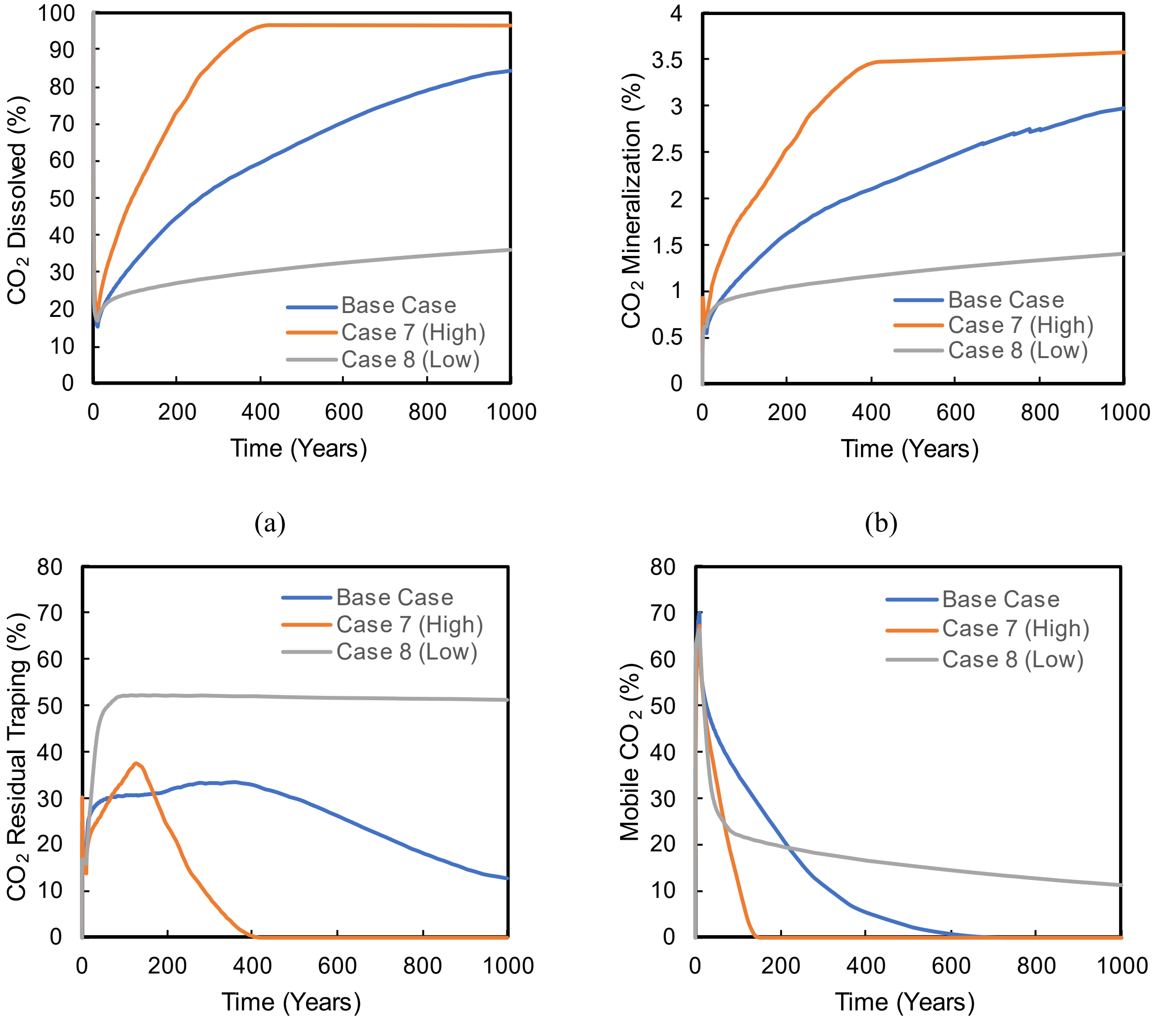

(a) (b)

(c) (d)

Figure 15. Effect of permeability in CO_2 trapping by (a) dissolution, (b) mineralization, (c) residual, and (d) mobile CO_2 after 1000 years of simulation.

However, during the early sequestration period, the fraction of CO_2 sequestered by different processes fluctuated significantly. Although the higher permeability case (case 7) dominates CO_2 dissolution and mineralization throughout the simulation, we observe a higher fraction of residual trapping in the low permeability case compared to the other cases after around 15 years of injection (**Fig. 16c**).

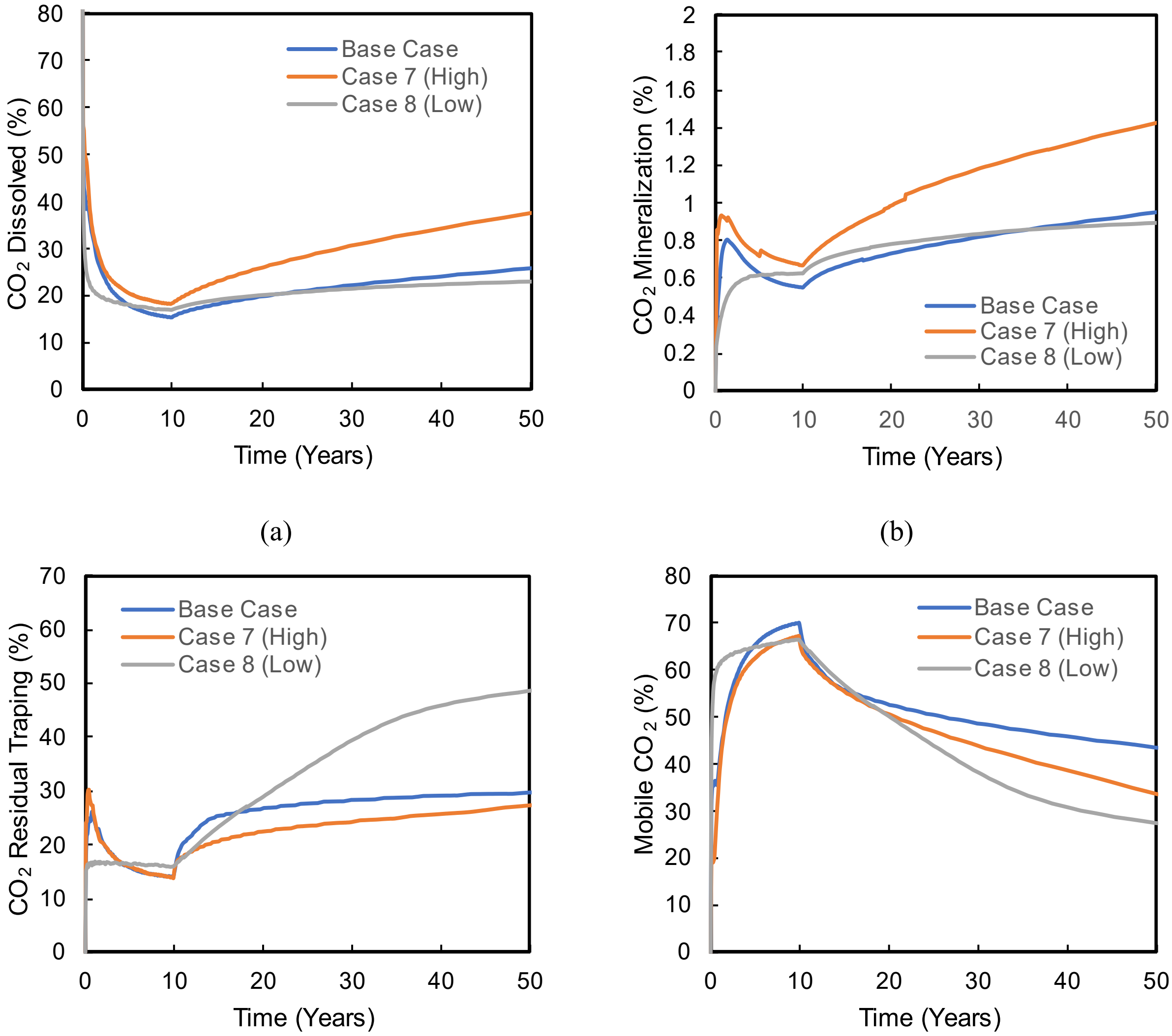

(a) (b)

(c) (d)

Figure 16. Effect of permeability in CO_2 trapping by dissolution, mineralization, residual, and mobile CO_2 (a), (b), (c), and (d) after 50 years of simulation.

The initial increase in residual trapping for case 8 (low permeability) can be attributed to the horizontal migration of CO_2 instead of vertical migration in the reservoir. This result is evident from the gas saturation plot in **(Appendix C.1, Fig. 27a-c).** For the low permeability case, shown in **(Appendix C.1, Fig. 27c)**, the gas saturation in the lateral direction is much higher than in high permeability cases. The lower permeability case also has a significant decrease in mobile CO_2 after 50 years of simulation, as shown in **Fig. 16d**, which results in a significantly lower fraction of CO_2 reaching the top of the aquifer, as observed in **Fig. 27c** (**Appendix C.1**).

We also observe that the halite precipitation is significantly higher in high permeability compared to low permeability **(Appendix C.2, Fig. 29a-c)**. The injected CO_2 increases the water vaporization for the high permeability reservoir, resulting in additional halite precipitation. This halite precipitation is most prominent near the injection well in all cases (base case, 7 and 8). Furthermore, as the permeability increases and more CO_2 migrates toward the upper layer of the reservoir below the caprock, more halite is observed to be precipitated below the caprock for the high permeability case (case 7). Halite precipitation is high at the leading edge of the CO_2 plume as the precipitated halite does not dissolve due to imbibition, as it does for prior grid blocks.

The results here show that the fraction of CO_2 sequestration by different mechanisms depends on the permeability of the reservoir. In low permeability zones, higher residual trapping is observed due to smaller pore spaces. However, high permeability zones promote enhanced dissolution and mineralization. Notably, the fraction of mobile CO_2 in the high permeability case is significantly lower than in the low permeability case after 1000 years, which is preferable for safe long-term storage of CO_2.

3.2.3 Effects of Porosity

The porosity of a reservoir is one of the most important parameters that determines its storage capacity. As the porosity of a reservoir can vary significantly, this is an important question that needs further evaluation. To investigate this, we conducted simulations by changing porosity and comparing the base case model (15% porosity) with two additional cases: one with lower porosity (8%) (case 9) and another with higher porosity (25%) (case 10). These values account for the porosity distribution in Mt. Simon sandstone, which falls within the range of approximately 10-25% [51]. The reservoir with smaller porosity reaches the maximum bottom-hole constraint before 10 years. Hence, to compare the results for the same cumulative injection, we run the simulations (including the base case) with 4 years of active injection, followed by 996 years of monitoring phase.

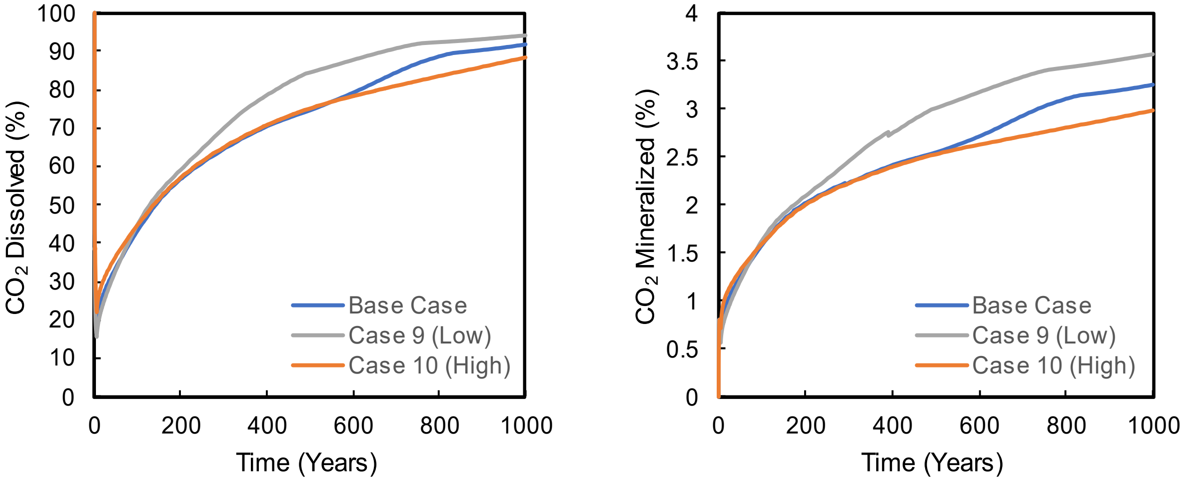

(a) (b)

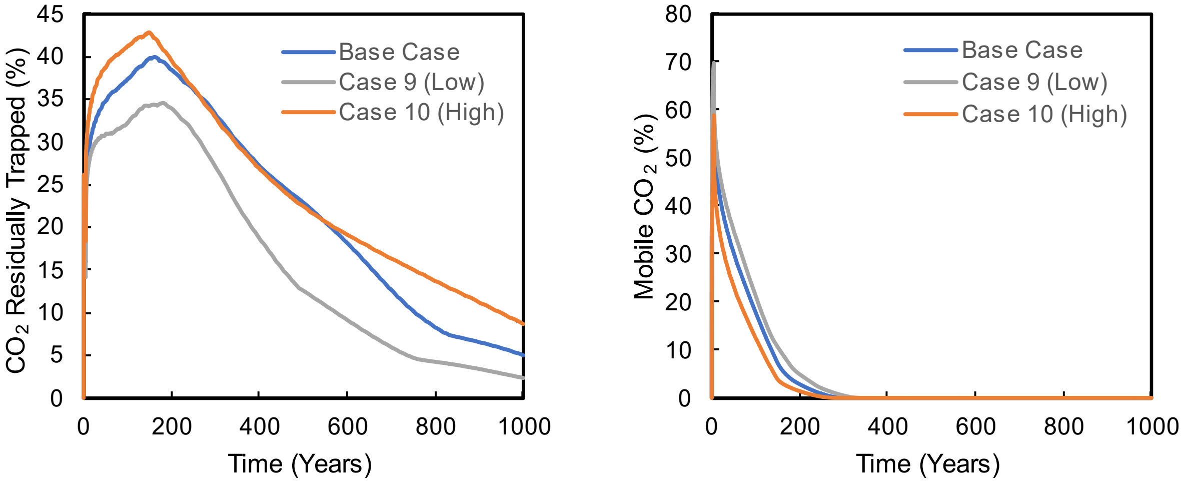

(c) (d)

Figure 17. Effect of porosity in CO_2 trapping by dissolution, mineralization, residual, and mobile CO_2 (a), (b), (c), and (d) after 1000 years.

Fig. 17a-d shows the effect of reservoir porosity on different trapping mechanisms. The low porosity case shows the highest fraction of CO_2 sequestered by dissolution and mineralization. However, the residual trapping is significantly lower in low-porosity cases. This difference can be attributed to the different pressure buildup in each reservoir. For the same cumulative gas injection, pressure in the low porosity case increases significantly more than in the high. As pressure-dependent Henry's constant controls the gas dissolution, the dissolution also increases. The mineralization rate also accelerates due to the reservoir's higher amount of aqueous CO_2. The increased fraction of dissolved and mineralized volume of CO_2 results in a lower amount of $ScCO_2$. Although the mobile phase $ScCO_2$ completely disappears in all the cases, **Fig. 17d** shows that it takes slightly longer (280 vs. 343 years) for the low porosity case. The bulk of the additional dissolved and mineralized CO_2 is derived from the residual phase, which is significantly lower in the low porosity case.

Next, we evaluate the halite precipitation and dissolution behavior as it can directly lead to further changes in porosity. The low porosity case has the maximum halite precipitation after 1000 years of simulation **Figure 16**. This result matches what was observed in **Fig. 17b**, where maximum mineralization was observed for the low porosity case. The reason for higher halite precipitation is a lower initial brine volume, which makes it easier to achieve the maximum salt concentration required for halite precipitation due to water vaporization.

Fig. 28a-c (Appendix C.1) shows that more CO_2 migrates towards the upper layer after 50 years of simulation in the low-porosity reservoir (case 9). This phenomenon is attributed to the conditions in case 9, where the limited pore spaces lead to a decrease in residual trapping of CO_2 and an increase in the concentration of mobile CO_2. Although a larger amount of halite precipitates for the higher porosity case close to the wellbore **(Appendix C.2, Fig. 29)**, a higher amount of halite precipitates throughout the reservoir, which is evident from **Fig. 29** (Appendix C.2**).**

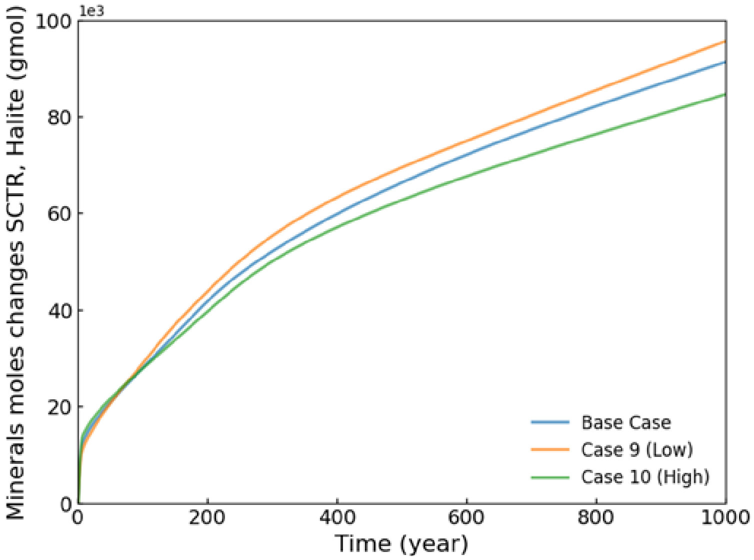

Figure 16. Halite concentration change (gmol) for different porosity reservoirs.

3.2.4 Effects of Initial Salt Concentration

Different formations have varying molality of salts, which can significantly impact the effectiveness of CO_2 sequestration in different storage sites. The initial molality of salts can affect the reservoir properties, the behavior of injected CO_2, and the overall storage capacity. To understand the impact of initial salt concentration on carbon storage by various mechanisms and the reservoir properties, we varied four major cations within a high and low range of concentrations reported for aquifers in different world regions [58]. In each case, an equal amount of CO_2 is injected over the same period, and the results are compared to the base case model. **Table 9** shows the initial salt concentration of $Na^{+}, Ca^{++}, K^{+}, Mg^{++}$ from low to high used in this study.

Table 9. Initial salt Concentration for sensitivity analysis

Salt	Low (mol/L)	Base (mol/L)	High (mol/L)
Sodium, (Na^{+})	1.087	1.8	3.045
Calcium, (Ca^{++})	0.161	0.47	0.938
Potassium, (K^{+})	0.031	0.036	0.639
Magnesium, (Mg^{++})	0.034	0.099	1.029

Figure 17a shows that the higher initial concentration of sodium (Na^{+}) ions lead to a significant reduction in the dissolved phase of CO_2, which was also observed in our prior studies [7]. However, the mineralization is slightly enhanced for the case with a higher concentration of Na^{+} ions. Although the presence of high Na^{+} ions lead to higher residual trapping of the injected CO_2, shown in **Figure 17c**; we observe that the mobile phase persists in the aquifer for a longer period of time (**Figure 17d**). For Mg^{++} and K^{+} ion, the percentage of dissolution trapping reduces by less than ~2.5% with the increase in concentration of these salts. Furthermore, the increase in concentration of Ca^{++} ions lead to a decrease in the percentage of dissolution trapping by ~4.5%. However, more residual and mineralized trapping of CO_2 is observed for high initial concentrations of Ca^{++} and Mg^{++}. These results are presented in **Fig. 30** (Appendix C.3).

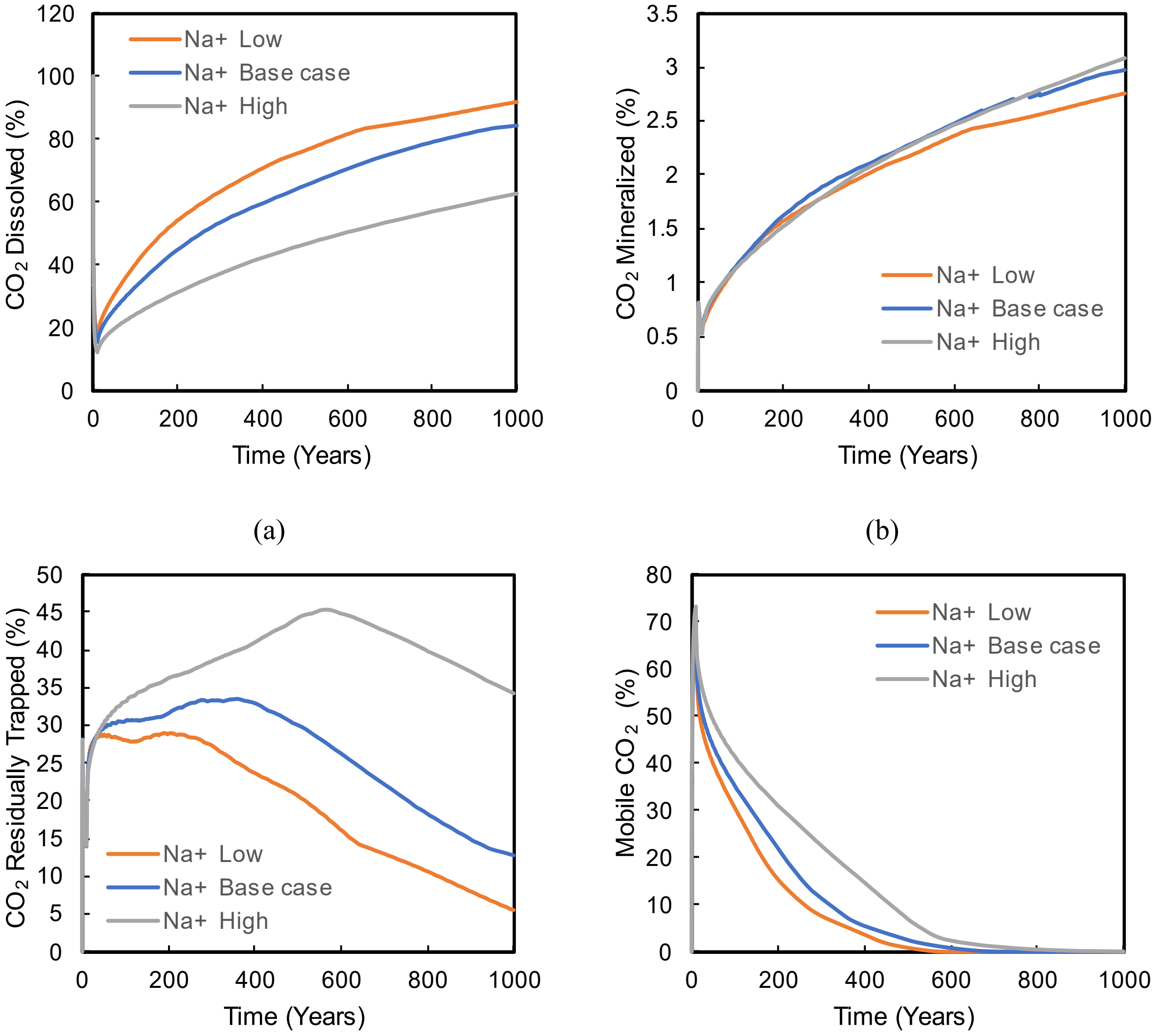

(a) (b)

(c) (d)

Figure 17. Effect of initial concentration of sodium ($\boldsymbol{Na^{+}}$) in CO_2 trapping by dissolution, mineralization, residual, and mobile CO_2 (a), (b), (c), and (d) after 1000 years.

Although altering the initial concentration of Ca^{++} and Mg^{++} ion slightly impact the percentage of dissolution trapping; results from the simulation showed that the concentration of Ca^{++} and Mg^{++} ions in the reservoir significantly influenced CO_2 mineralization due to the precipitation of calcite and dolomite **(Appendix C.3, Fig. 31)**. While both dolomite and calcite require Ca^{++} ions for precipitation, dolomite has an additional requirement for Mg^{++} ions alongside Ca^{++}. So, the abundance of Ca^{++} ion leads to preferential precipitation of calcite, as shown in **Figure 18a**. In addition, it is observed that the precipitation rate of dolomite increases with the increase of Mg^{++} concentration (**Figure 18b**). However, **Figure 18b** also shows that calcite dissolves under conditions where there is a higher concentration of Mg^{++} ions.

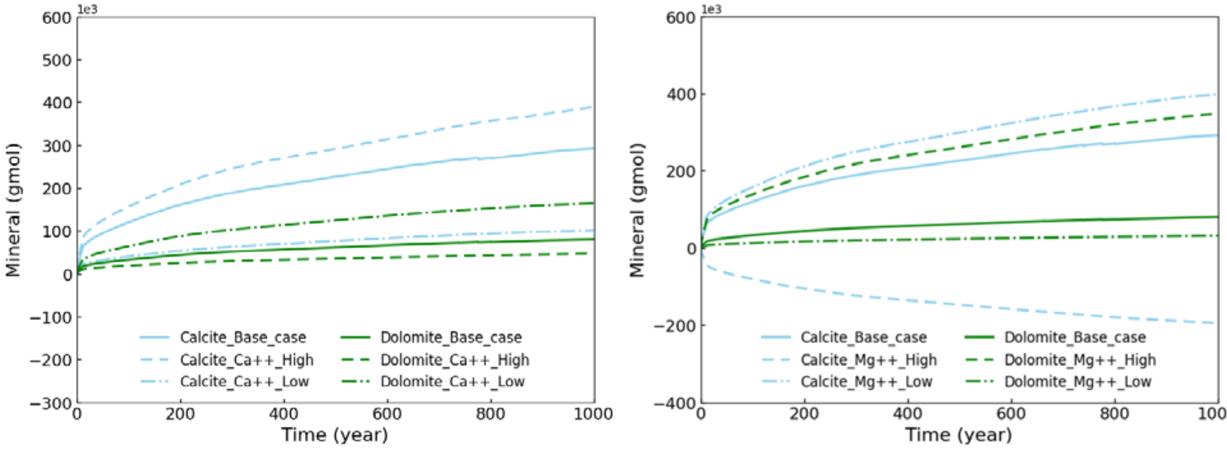

(a) (b)

Figure 18. Effects of initial **concentration** of (a) $\boldsymbol{Ca^{++}}$ and (b) $\boldsymbol{Mg^{++}}$ ion **on calcite** and dolomite precipitation.

Figure 19 shows that the higher initial sodium (Na^{+}) concentration leads to more halite precipitation throughout the reservoir. We also see that because of halite precipitation near the injection well, the porosity decreases, resulting in the highest decrease in porosity for a high initial concentration of Na^{+}, however, the rest of the reservoir experiences a slight increase in porosity. The rate of kaolinite dissolution, the only mineral that dissolved in our simulation, is high in the case with a high initial concentration of Na^{+}.

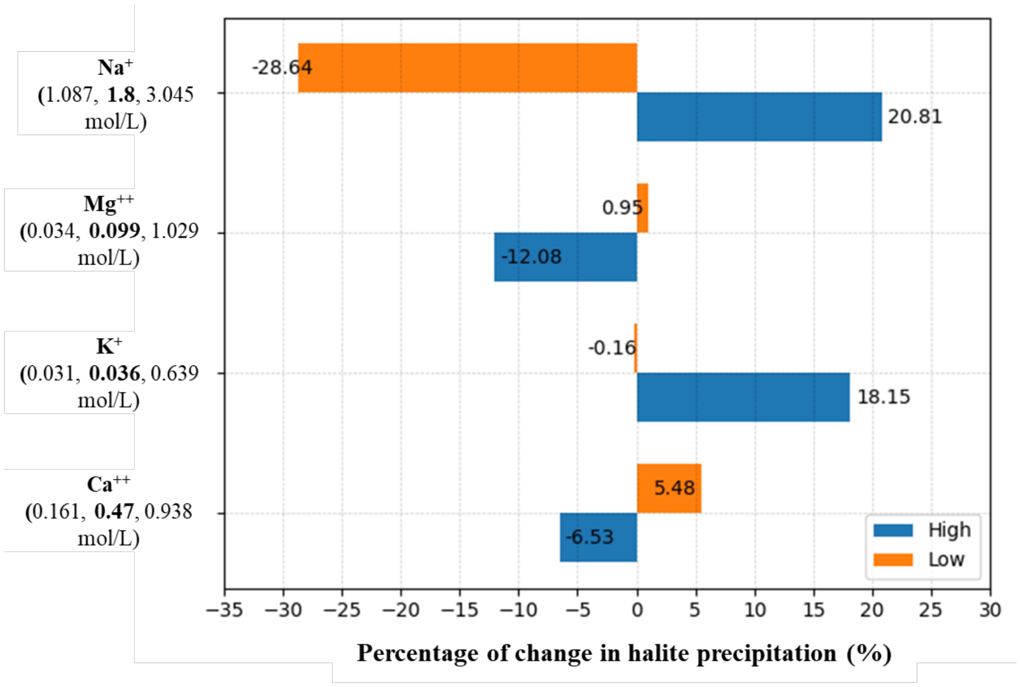

**Salt concentration values in the y-axis follow the format of "Salt Type (Lowest Concentration, Base Case Concentration, Highest Concentration)"*

Figure 19. Percentage of change in halite precipitation with change in initial salt concentration for 1000 years of simulation.

Kaolinite dissolution releases Al^{3+} and SiO_2, which then interact with the abundant Na^+ and SiO_2 present in the solution, leading to the formation of albite. As the activation energy for albite precipitation is less than that of quartz, a greater amount of SiO_2 is utilized for albite precipitation; as a result, less amount of quartz precipitation is observed in the case with a high initial concentration of Na^+. The reduced quartz and enhanced kaolinite precipitation increases porosity across the reservoir, except in the injection area. It is observed that with an increase in initial. K^+ ion, precipitation of halite increases, as shown in **Figure 19**. An opposite trend is observed for the initial concentration of Mg^{++} and Ca^{++} ions, with an increase of these ions, the precipitation of halite decreases.

3.2.5 Effects of Reactive Surface Area

Reactive surface area (RSA) represents the average available surface area for the mineral reaction within the porous media. RSA is a dynamic property of minerals that changes over time and is highly influenced by the distribution of heterogeneity, diverse shapes, and intricate contact interfaces of the minerals [45]. RSA is a crucial input parameter in reactive transport modeling as it directly impacts the magnitude of mineral trapping in long-term CO_2 storage [43]. RSA values are typically calculated using specific surface area (SSA). In this study, the maximum and minimum values of individual minerals' RSA are calculated using the SSA values reported in the literature. **Table 10** lists the ranges of RSA of minerals used in this study. In total, 21 extra case simulation cases were conducted to explain the effects of RSA.

Table 10. Range of RSA for the minerals used in this study.

Mineral	RSA range (m^2/m^3)	Reference
Quartz	32,197 – 158,841	[10]
Albite	1846 - 7570	[10]
Calcite	320 – 37,852	[91]
Dolomite	146,799 – 193,885	[92–94]
Kaolinite	219,505 – 914,027	[10]
K-feldspar	81,223 – 240,625	[10]
Siderite	369,744 – 707,2234	[91]

Results from our simulations show that CO_2 mineralization is significantly affected by the RSA of quartz and moderately by the RSA of albite. When the reactive surface area of quartz is increased by approximately 393%, from 32,197 to 158,841 m^2/m^3, a substantial increase in CO_2 mineralization of around 161% is observed, as shown in **Figure 22**. These findings are also reported in prior studies by Bolourinejad et al. [74], where the surface area of quartz was found to have the largest effect on the amount of mineralized CO_2. Other than quartz, the increase of RSA of albite also slightly impacts its precipitation behavior. Increasing the RSA of albite by ~310% leads to a modest 13% increase in CO_2 mineralization. Apart from quartz and albite, minimal change in precipitation and dissolution behavior is observed in response to the variations of the RSA of other minerals. Similar results were obtained in prior studies [74,75], where only the RSA of quartz and feldspar groups showed any impact on precipitation and dissolution of the respective minerals.

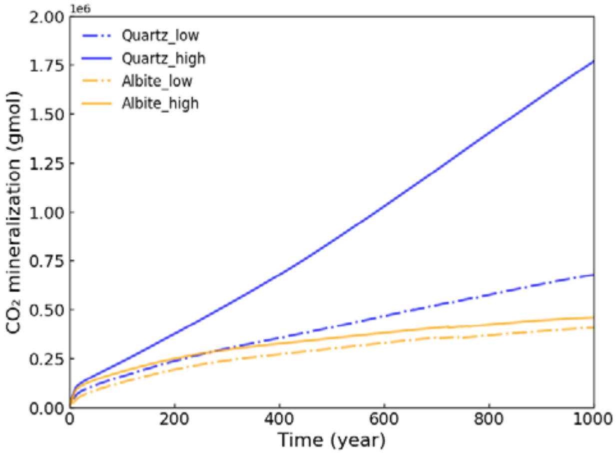

Figure 20. Effect of RSA of quartz and albite on CO_2 mineralization

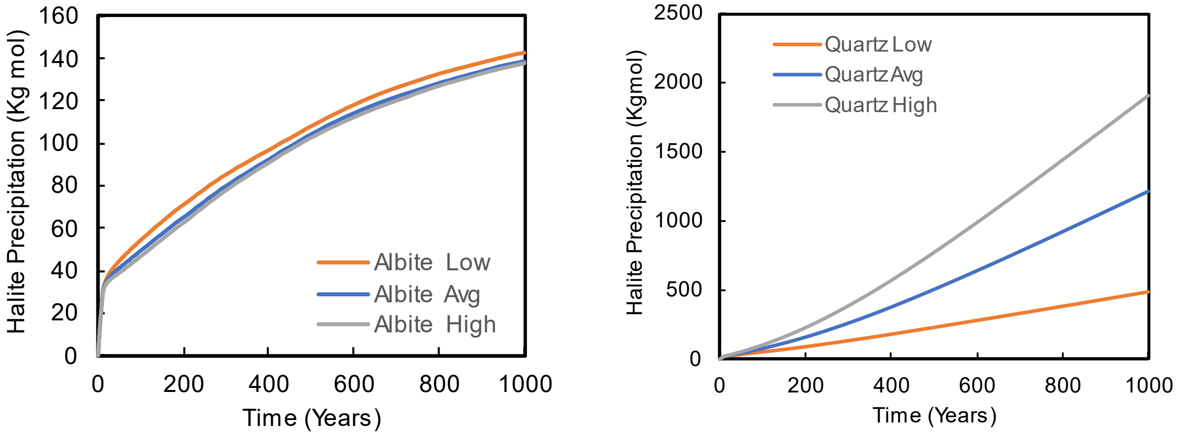

(a) (b)

Figure 21. Effect of the reactive surface area of (a) albite and (b) quartz on halite precipitation.

Quartz and albite have a substantial impact on the precipitation of halite and the porosity of the reservoir presented in **Figure 21**. Higher precipitation of quartz decreases the concentration of SiO_2 in the brine; thus, more albite dissolution occurs for equilibrium. Dissolution of albite releases Na^+ which eventually facilitates halite precipitation. On the other hand, when the reactive surface area (RSA) of albite is enhanced, there is a rise in albite precipitation through the consumption of Na^+, SiO_2 and Al^{3+} ions. This leads to a decrease in the concentration of Na^+ ions in the brine, consequently lowering halite precipitation.

4. Discussion

Although there has been significant research on CO_2 subsurface storage, some focus areas require further investigation. In this context, this study provides a structured, comprehensive overview of CO_2 trapping in saline aquifers, addressing the effect of different operating and geophysical parameters on CO_2 trapping behavior. Furthermore, the mineral dissolution/precipitation behavior and its effect on the reservoir properties are discussed. This section discusses the key findings of this study.

4.1. Implications of P_c and K_r on CO_2 storage and reservoir flow properties

Based on the base case simulation results, although CO_2 is trapped as a mobile phase in the initial sequestration stage, residual and dissolution trapping becomes dominant in the later stages. After 684 years, almost all the mobile CO_2 is dissolved, which is desirable since CO_2 trapped underneath caprocks has the highest potential to leak through undetected or reactivated fractures. Furthermore, dissolution trapping is the primary trapping mechanism since almost half of the injected CO_2 is stored via dissolution trapping in just 300 years, and at the end of 1000 years, around 80% of the injected CO_2 is sequestered (**Figure 4**). The second most dominant trapping mechanism is residual trapping, sequestrating around 27% of injected CO_2 at the end of 1000 years. Although, at the end of 1000 years, a negligible fraction of total injected CO_2 (2.97%) is sequestered in the forms of solid precipitates, dissolution/precipitation of carbonates and other minerals changes the flow properties of the reservoir. The capillary pressure is the most significant trapping mechanism for CO_2 storage security as it promotes both residual trapping and dissolution trapping (**Figure 6**). When capillary pressure is included, higher mineralization and dissolution compared to the cases without capillary pressure (**Figure 6**). The capillary pressure creates disconnected ganglia of CO_2 throughout the reservoir which increases the concentration gradient required for both dissolution trapping and mineralization trapping. The most significant implication of capillary pressure is the immobilization of the injected CO_2, without which close to 50 % of the injected CO_2 remains in the mobile phase (**Figure 6**).

Calcite and dolomite are identified as the two major minerals contributing to the formation of carbonate precipitates. After 1000 years, kaolinite was the only mineral that dissolved, while the other minerals precipitated due to their interaction with the injected CO_2 and brine. Furthermore, the impact of halite precipitation is only significantly close to the wellbore. This is due to water vaporization, which leads to salting out due to the high concentration of NaCl in brine. The halite precipitation can significantly reduce the permeability (as high as 34%, **Figure 9**.). This reduction in the near wellbore permeability can affect the injectivity of the reservoir. However, although the porosity/permeability was reduced around the wellbore, we observed an increase in the porosity/permeability throughout the other reservoir regions [68,69].

4.2. Effect of Varying Decision and Uncertain Parameters

Aside from the base case simulation, we observe that various decisions and uncertain parameters critically impact CO_2 storage by different mechanisms. The key findings of the sensitivity studies are summarized and tabulated in **Table 11**.

Table 11. Major observations on the effect of operational and geophysical parameters in CO_2 storage behavior

Key Parameters	Major observation
Injection rate	• A low injection rate increases the percentage of CO_2 dissolved in the reservoir. • A moderate injection rate will lead to a faster accumulation of carbon credits and reduce the halite precipitation near the injection well.
Permeability	• Reservoirs with high permeability will increase CO_2 dissolution and mineralization. • High permeability reduces the fraction of mobile CO_2, which is preferable for long-term storage.
Porosity	• Reservoir with higher porosity will increase the residual trapping of CO_2 • Mobile phase $ScCO_2$ will disappear faster in the reservoirs with high porosity.
Initial salt concentration	• Ca^{++} and Mg^{++} has a significant effect on CO_2 mineralization, reservoirs with higher initial concentrations of these ions will precipitate more calcite and dolomite. • Na^{+} significantly impact halite precipitation, higher initial concentration of Na^{+} will lead to high halite precipitation.
Reactive surface area (RSA)	• Compared to other minerals, the RSA of quartz significantly affects the CO_2 mineralization, whereas the RSA of albite has a moderate impact.

The highest injection rate leads to the least fraction of mobile CO_2 in a reservoir. This is mainly because relative permeability hysteresis and capillary pressure are also in effect sooner at a high injection rate. Although not the scope of this study, the geomechanical aspects of high injection rates must be accounted for since high injection rates can lead to high reservoir pressure buildup, which might compromise the storage integrity of the saline aquifer. As shown in **Table 11**, CO_2 injection in highly permeability saline aquifers is preferable, as higher permeability promotes enhanced dissolution and mineralization. This is because the injected CO_2 encounters a higher volume of fresh brine, maintaining the high concentration gradient required for dissolution and mineralization. For the same reason, a reservoir with high porosity is preferred as the injected CO_2 can quickly react with a large volume of brine, leading to a comparatively lower fraction of the mobile phase.

The salt type and concentration in saline aquifer fluids also influence the CO_2 trapping behavior. The results suggest the concentration of Ca^{++} and Mg^{++} ions in the reservoir significantly influenced CO_2 mineralization due to the precipitation of calcite and dolomite, whereas a higher Na^{+} and initial K^{+} concentration leads to more halite precipitation throughout the reservoir. Furthermore, as observed from the reactive surface area study, the RSA of quartz significantly controls the CO_2 mineralization rate. Other than quartz, the RSA of albite also moderately controls the mineralization rate. The RSA of other minerals did not significantly change the mineralization rate, which was also observed in other studies [74].

4.3. Limitations and Future Work

This study offers a comprehensive insight into the critical aspects of CO_2 subsurface storage, taking into account the effects mineral precipitation and dissolution reactions, and changes in the porosity and permeability of the system for 1000 years. One of the limitations of this study is the lack of distinction between the reservoir and caprock mineralogical profile. Including such distinction can provide critical insights that will help understand the potential of CO_2 leakage due to its interaction with the caprock. Although not a scope of this study, future work will also consider sensitivity studies involving capillary pressure and relative permeability curves. As there are many uncertainties from formation to formation, such studies would provide valuable insight to understand the flow behavior of CO_2 in subsurface formations. Furthermore, this study assumes no impurities in primary minerals, and the impact of secondary minerals and capillary pressure hysteresis is considered negligible. Finally, a mineralization study encompassing a wide range of primary and secondary minerals focusing on reaction rate constants can provide further insight into the geochemical aspects of CO_2 storage.

5. Conclusions

This study provides a structured, comprehensive overview of the various aspects of CO_2 sequestration in deep saline aquifers, addressing the effect of different operating and geophysical parameters. Specific focus is placed on understanding the impacts of capillary pressure and relative permeability hysteresis on dissolution and mineralization trapping. Furthermore, the mineral dissolution/precipitation behavior and its effect on the reservoir properties are discussed. The key findings are summarized as follows.

- Capillary plays a critical role in sequestering CO_2 injected into deep saline aquifers by enhancing both dissolution and mineralization trapping. When capillary pressure are ignored, almost half of the injected CO_2 stays in the reservoir in the mobile phase.
- Mineralization trapping in sandstone formation is not a major mechanism for CO_2 storage with less than 4% of the injected CO_2 existing as mineral precipitates for the mineralogy and aquifer brine considered in this study. However, dissolution and precipitation of various minerals play a crucial role in CO_2 sequestration as they can change the flow properties of the reservoir. The reservoir property change can be significantly close to the wellbore due to halite precipitation.
- The mineralization behavior of calcite and dolomite contributes significantly to forming carbonate precipitates. While considering the dissolution/precipitation behavior, all the minerals except kaolinite precipitated during interaction with the injected CO_2 and brine.
- Mobile phase CO_2 is observed to disappear faster in saline aquifers with high permeability and porosity. Furthermore, although a high CO_2 injection rate can translate to higher dissolution and mineralization trapping, the geomechanical aspects must be considered beforehand.
- CO_2 mineralization trapping is significantly influenced by the RSA of quartz and the concentration of Ca^{++} and Mg^{++} ions, whereas a higher Na^{+} and initial K^{+} concentration leads to more halite precipitation throughout the reservoir.

A. Khanal, M. Irfan Khan, M. Fahim Shahriar, Comprehensive Parametric Study of CO2 Sequestration in Deep Saline Aquifers, Chem. Eng. Sci. (2024) 119734. https://doi.org/10.1016/j.ces.2024.119734.

Acknowledgements:

We thank the anonymous reviewers for their edits and suggestions, which improved our manuscript. This material is based upon work supported in part by the National Science Foundation Award under CBET-2245484 and in part by the U.S. Department of Energy, Office of Science, Basic Energy Sciences' Geoscience program under Award Number DESC0024642. Any opinions, findings, conclusions, or recommendations expressed in this material are those of the author(s) and do not necessarily reflect the views of the funding agencies.

Appendix A. Mathematical Description

A.1. Governing Equation

The governing equation for the reactive transport processes in this study is the coupled mass and momentum conservation equations. The accumulation of CO_2 results from the combined effects of convective mass transfer, diffusive/dispersive mass transfer, chemical reaction consumption/production, and the mass of the injected gas [1,5]. The material balance equation for fluid flow of component $i = \{CO_2, H_2O, Salt, \dots\}$ and phase β is expressed as -

$$\sum_{\beta}\frac{\partial}{\partial t}\,\rho_\beta\varphi S_\beta m_\beta^i = \sum_{\beta}\nabla.\,\left(\rho_\beta u_\beta m_\beta^i + j_\beta\right) + r^i + \psi_\beta^i \tag{A.1}$$

Where, φ is the porosity, ρ denotes the phase density, S represents the phase saturation, m is the phase mass fraction of the i^{th} component, j_β represents non-advective flux vector for component i in phase β, ψ_β^i is the external sources or sinks of mass for component i in phase β, r^i is the reaction of the i^{th} component and u_β is the Darcy or convective flux and usually written as-

$$u_\beta = -\frac{K_{r,\beta}K}{\mu_\beta}\,.\left(\nabla p_\beta - \rho_\beta g\right) = -\lambda_\beta K\,.\left(\nabla p_\beta - \rho_\beta g\right) \tag{A.2}$$

Where, $K_{r,\beta}$ is relative permeability, K is intrinsic permeability tensor, λ_β is the phase mobility, g is the gravitational acceleration vector, p_β is the phase pressure.

The gas density is calculated with the Peng and Robinson equation (PR-EOS) [76], and the aqueous phase density and viscosity are calculated by Rowe and Chou [77] and Kestin et al. [78] correlation, respectively.

It is assumed that gaseous and aqueous phases are in a state of thermodynamic equilibrium. Mathematically it can be expressed as the quality of the fugacity of the component in the gaseous and aqueous phases. The equation can be expressed as:

$$g_i = f_{ig} - f_{iw} = 0, \qquad i = 1, \dots., n_c \tag{A.3}$$

Where, $f_{ig}$and f_{iw} represents the fugacity of component i in the gas and aqueous phase. n_c is the number of gaseous components. The fugacity f_{ig} is calculated using the PR-EOS [76]. Henry's law is used to calculate the fugacity, f_{iw} of gaseous components soluble in the aqueous phase [79], i.e.

$$f_{iw} = y_{iw} \times H_i \tag{A.4}$$

Henry's constant H_i are functions of pressure, temperature, and salinity. The variation of Henry's law constants based on reservoir pressure and temperature are modeled by using Harvey correlation [80] and the effect of salinity is modeled by using the correlation given in Cramer [81]:

$$\log_{10}\left(\frac{H_{i,salt}}{H_i}\right) = K_{salt}m_{salt} \tag{A.5}$$

where $H_{i,salt}$ is the Henry's constant of CO_2 in brine, H_i as described above is the Henry's constant at zero salinity, k_{salt} is the salting-out coefficient, and m_{salt} is the molality of dissolved salt. The, k_{salt} is calculated by using the method described in Bakker [82].

Complete vaporization of H_2O may take place which can affect the CO_2 injectivity, and to model H_2O vaporization **Eq. A.3** is applied to the H_2O component [83]. i.e.

$$g_{n_c} = f_{H_2O,g} - f_{H_2O,aq} = 0 \tag{A.6}$$

The fugacity $f_{H_2O,g}$ is calculated from the cubic EOS and the fugacity $f_{H_2O,aq}$ calculated using the Canjar and Manning [77,84,85], and Saul and Wagner [77,84,85].

The molecular diffusion of CO_2 in brine is modeled using the Fick's second law described in **Eq. A.7** [86].

$$\frac{\partial c}{\partial t} = D\,\nabla^2 c \qquad \text{(A.7)}$$

Where, c denotes the concentration of a component, and D is Fick's diffusion coefficient.

A.2. Geochemical Reactions

Considering, n_m, n_{aq} as the total number of mineral and aqueous phase components, respectively and n_{ct} is the total number of components in gaseous, aqueous, and mineral phase. Then the stoichiometry equation for the reaction between the aqueous phase species is [83]-

$$\sum_{k=1}^{n_{aq}} v_{k\alpha}^{a}\, A_k = 0\,, \qquad \alpha = 1, \dots, R_{aq} \qquad \text{(A.8)}$$

Where, $v_{k\alpha}^{a}$ is the stoichiometric coefficient of aqueous component k in reaction α. R_{aq} is the number of reactions between aqueous components and A_k is the chemical symbol for the k^{th} aqueous species.

The stoichiometry equation for the reaction for mineral dissolution/precipitation is [83]-

$$\sum_{k=1}^{n_{ct}} v_{k\beta}^{m}\, A_k = 0\,, \qquad \beta = 1, \dots, R_{mn} \qquad \text{(A.9)}$$

Where, $v_{k\beta}^{m}$ is the stoichiometric coefficient of mineral component k in reaction β. R_{mn} is the number of reactions between minerals and aqueous components.

As the reactions between species in the aqueous phase are fast compared to the mineral dissolution/precipitation reactions, the intra-aqueous reactions can be represented as the chemical equilibrium equations. In contrast, the mineral dissolution/precipitation reactions are considered as rate-dependent reactions.

The governing equation for chemical equilibrium reactions are [46]-

$$Q_\alpha - k_{eq,\alpha} = 0, \qquad \alpha = 1, \dots, R_{aq} \qquad \text{(A.10)}$$

With

$$Q_\alpha = \prod_{k=1}^{n_{aq}} a_k^{v_{k\alpha}} \qquad \text{(A.11)}$$

Here, $k_{eq,\alpha}$ represents the chemical equilibrium constants for each reaction. $Q_\alpha, v_{k\alpha}$ and a_k are the activity product, stoichiometry coefficients, and activity of component k, respectively. The B-dot model is used to calculate the activity coefficients [87].

A.3. Mineral Dissolution/precipitation and Porosity-permeability Relationship

The rate law for the mineral dissolution/precipitation reaction equation is [88] –

$$r_j = \widehat{A}_j\, k_j \left(1 - \frac{Q_j}{k_{eq,j}}\right), \qquad j = 1, \dots, R_{mn} \qquad \text{(A.12)}$$

where, r_j represents the reaction rate, $\widehat{A_J}$ is the reactive surface area, k_j denotes rate constant, $k_{eq,j}$ is the equilibrium constant and Q_j is the activity product analogous to the aqueous chemical equilibrium reactions equation (**Eq. A.11**). The procedure for calculating each of these parameters are described by Ngheim et al. [46]. The ratio $\frac{Q_j}{k_{eq,j}}$ is called saturation index of the reaction. If the saturation index is higher than 1, then mineral dissolution occurs and if it is less than 1 then mineral precipitates.

The reactive surface area, $\widehat{A_J}$ is a crucial parameter for the calculation of the rate**. Eq. A.13** is utilized to compute the reactive surface area with changes in the number of moles of minerals due to dissolution or precipitation [46].

$$\widehat{A_J} = \widehat{A_J}^0 . \frac{N_j}{N_j^0} \tag{A.13}$$

Here, $\widehat{A_J}^0$ represents the reactive surface area at time zero. N_j, N_j^0 are the mole number of mineral j per unit grid block volume at the current time and when time is zero, respectively. The void volume of the porous medium changes because of mineral dissolution/precipitation. The change in porosity, φ because of mineral dissolution/precipitation, is updated in each time step, measured from the mineral volume fraction of the current time [46], as follows:

$$\hat{\varphi}^* = \varphi^* - \sum_{j=1}^{n_m} \left(\frac{N_j}{\rho_j} - \frac{{N_j}^0}{\rho_j} \right) \tag{A.14}$$

$$\varphi = \hat{\varphi}^* \left[1 + c_\varphi (p - p^*) \right] \tag{A.15}$$

Where, φ denotes the porosity, $\hat{\varphi}^*$ represents the reference porosity, including mineral precipitation/dissolution, φ is the reference porosity without mineral dissolution and precipitation, $N_j, {N_j}^0$ represents the total moles of mineral j per unit grid block volume at the current time and when time is zero, respectively. ρ_j, c_φ and p^* are the mineral molar density, rock compressibility, and reference pressure, respectively.

Changes in permeability induced by mineral dissolution and precipitation can be measured using experimental relationships or analytical models between porosity and permeability. The Kozeny-Carman (K-C) equation measures permeability [46].

$$\frac{k}{k^0} = \left(\frac{\varphi}{\varphi^0} \right)^{\xi} . \left(\frac{1 - \varphi^0}{1 - \varphi} \right)^2 \tag{A.16}$$

Where, k^0 and φ^0 denotes the initial permeability and porosity, respectively and ξ is the Kozeny-Carman exponent.

A.4. Relative Permeability and Capillary Pressure

The relative permeability curves for water and gas were generated using the Brooks-Corey function [61]. The drainage section of the relative permeability curve for the water and gas phase is derived from the following equations.

$$S_w^* = \left(\frac{S_w - S_{wi}}{1 - S_{wi}} \right) \tag{A.17}$$

$$k_{r,w} = (S_w^*)^{N_w} \tag{A.18}$$

$$k_{r,g} = \left[k_{r,g}(S_{wi})\right](1 - S_w^*)^2\,[(S_w^*)^{N_g}] \tag{A.19}$$

Where, S_w^* denotes normalized water saturation and S_w is water saturation. S_{wi} is irreducible water saturation, and the value is 0.22 [53]. $k_{r,w}$ and $k_{r,g}$ represents the relative permeability of water and gaseous phase, respectively. N_g and N_w is known as the Corey exponent and reflects pore-size distributions. In this study, the value of N_g and N_w is set to 4 and 9, respectively, and the value of $k_{r,g}(S_{wi})$ is assumed to be 0.95 [53].

Residual gas saturation (S_{gr}) strongly depend on the initial gas saturation (S_{gi}) and can be obtained using Land's formula:

$$\frac{1}{S_{gr}^*} - \frac{1}{S_{gi}^*} = C = \frac{1}{S_{gr(Swi)}} - \frac{1}{S_{wi}} \tag{A.20}$$

$$S_{gi}^* = \frac{S_{gi}}{1 - S_{wi}}\ ;\ S_{gr}^* = \frac{S_{gr}}{1 - S_{wi}}\ and\ S_g^* = \frac{S_g}{1 - S_{wi}} \tag{A.21}$$

where, S_g^*, S_{gr}^* and S_{gi}^* are the normalized gas saturation, normalized residual gas saturation (0.21 in this study), and normalized initial gas saturation, respectively. C is the Land coefficient which is 2.1 obtained from Krevor et al. [53]. Land considered a status with mobile non-wetting phase saturation (S_{gf}^*), using the following equation (S_{gf}^*) can be calculated for different gas saturations.

$$S_{gf}^* = \frac{1}{2}\left(S_g^* - S_{gr}^* + \sqrt{\left(S_g^* - S_{gr}^*\right)^2 + \frac{4}{c}\left(S_g^* - S_{gr}^*\right)^2}\right) \tag{A.22}$$

By placing the value of S_{gf}^* calculated from **Eq. A.22** in the following relation, the gas relative permeability can be obtained-

$$K_{rgi} = S_{gf}^{*2}\left(1 - \left(1 - S_{gf}^*\right)^{\epsilon - 2}\right) \tag{A.23}$$

Here, K_{rgi} represents the imbibition relative permeability and exponent $\epsilon = \frac{2}{\lambda} + 3$, where λ is the pore size distribution, and the value is 0.55 for Mt. Simon sandstone [53].

The Brooks-Corey equation [61] is also used to obtain the capillary pressure for drainage $(p_{c,d})$.

$$p_{c,d} = p_e\left(\frac{S_w - S_{wi}}{1 - S_{wi}}\right) \tag{A.24}$$

Where, p_e is the capillary entry pressure which is 4.6 kPa as reported in Krevor et al. [53].

Appendix B. Grid Size Sensitivity and Effect of Volume Modifier

B.1. Study of Grid Size Sensitivity

The grid size in a numerical reservoir simulation model should be sufficiently small to minimize numerical dispersion, material balance error and improve simulation convergence. However, when the grid sizes are too small, the computational time increases significantly for a compositional simulation model with geochemistry enabled. Hence, we evaluate the model's applicability in the base case by considering an additional simulation case with additional grid refinement. The refined model (case 4) uses 6734 grid blocks (259 x 1 x 26), which is 66% higher than the number of grid blocks used in the base case (4060, 203x1x20).

The five central grid blocks in the I-direction have dimensions of 0.79 m, and the remaining 254 grid blocks, 128 on each side, range from 1 m close to the wellbore and 10 m in the outer boundary, which are spaced between $10E(\log_{10}(1))$ and $10E(\log_{10}(10))$. Similarly, in the K direction, the 25 grid blocks are uniformly spaced between $10E(\log_{10}(1))$ and $10\mathrm{E}(\log_{10}(10))$. The bottommost grid is assigned a size of 0.6204 m, so the reservoir thickness is 100m, as in the base case. For both cases, the same amount of CO_2 is injected over 10 years, and then the migration of CO_2 is monitored for the next 990 years. **Fig. 24** shows the amount of CO_2 trapped by different mechanisms during the simulation period. The visual inspection of the results shows a very good match between the base case model and the refined model for all the trapping mechanisms.

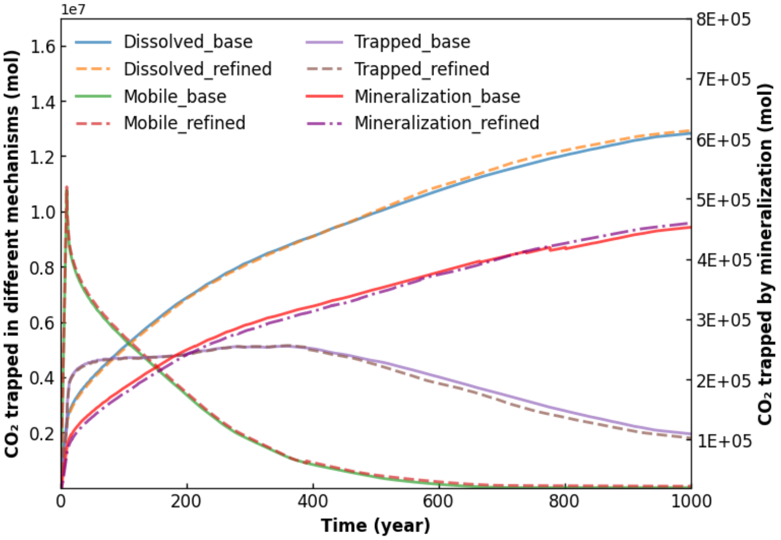

Figure 24. Comparison of CO_2 trapped by different mechanisms (a) dissolution, mobile and trapping, (b) mineralization, calculated from the base case and the refined case.

We also calculated the average absolute error for each trapping mechanism as follows:

$$\left|\frac{Base\ case\ -\ Refined\ case}{Refined\ case}\right| \times 100\%$$

The various error metrics calculated for the simulation are summarized in **Table 12**.

Table 12. Error comparison between the base case and refined case (case 4)

	CO_2 Dissolved	CO_2 Mineralized	Supercritical CO_2
Average error (%)	1.10	2.82	2.82
Maximum error (%)	6.66	30.80	7.62
Final year error (%)	0.78	1.5	5.19

Table 12 shows that the limited number of grid blocks in the base case produces similar results as a computationally more expensive refined case. The mineralization initially shows a relatively high error as the mineral precipitation and dissolution is very slow, resulting in ill-conditioned behavior during the early simulation period. However, the error decreases significantly, and the final error for all the trapping mechanisms is less than 6%. We observe a negligible gain in accuracy even with a significant increase in grids and additional computational time. Hence, base case simulation is selected in this study.

B.2. Effect of Volume Modifier

The simulations in this study do not use volume modifiers, usually implemented in the grids at the outer boundaries of a numerical reservoir model, to model an infinite-acting reservoir [89,90]. A volume modifier artificially increases the porosity of the grid blocks so that the actual pore volume is higher by the factor assigned by the volume modifier. This technique enables a high injection rate with only a modest increase in reservoir pressure. However, this setup does not always capture the expected physical processes when CO_2 is injected into a reservoir. As the dissolution is controlled by the fugacity of the solute (CO_2) in the two phases (**Eqn. 3-4**), the injected $ScCO_2$ dissolves instantaneously when it encounters the grid block with an artificially increased volume modifier with a large volume of brine and no dissolved solute.

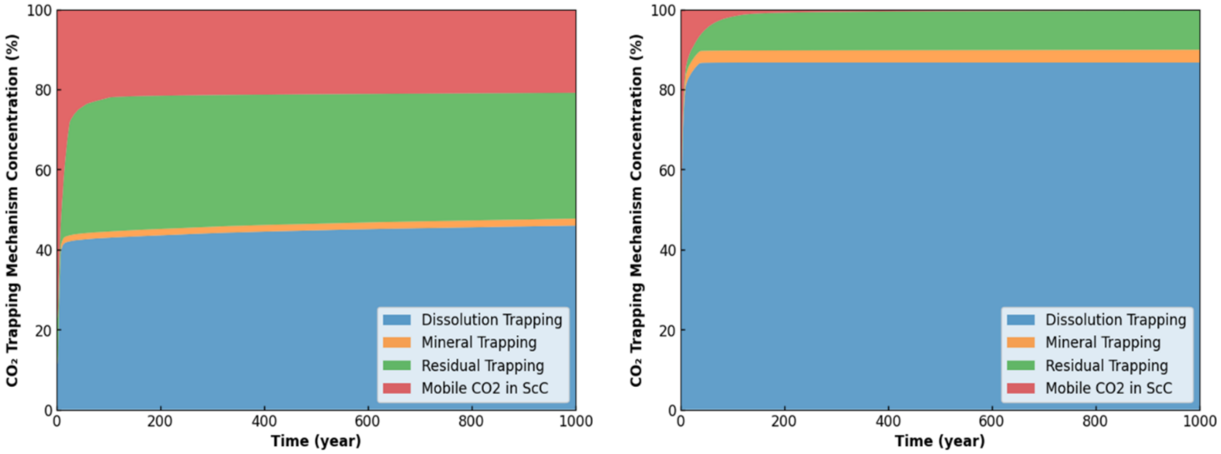

(a) (b)

ScC: Supercritical Condition

Figure 25. Contribution of different trapping mechanisms of CO_2 by implementing volume modifiers (a) 1000 and (b) 5000 at the outer boundaries.

This is not a realistic behavior because if a larger number of grids were used to model the equivalent porosity, the dissolution rate would be controlled by the time it takes for $ScCO_2$ to move from one grid to the other grid blocks. Thus, using a volume modifier results in a sharp increase in dissolution as soon as it reaches the modified grid block. To verify this, we simulated two additional cases, Vm-1000 and Vm-5000, where the outermost grid blocks in the I-direction are assigned a volume modifier of 1000 and 5000, respectively. The injection rate for the grid blocks is selected based on the total volume of CO_2 in standard conditions stored in the reservoir after ten years of active injection period, as shown in **Table 13.**

Table 13. Parameters used in volume modifier case study.

Case	Base Case	Vm-1000	Vm-5000
Volume modifier	1	1000	5000
Average porosity	0.15	0.15	0.15
Total bulk volume (m^3)	2.0×10^5	4.2×10^6	2.0×10^7
Total pore volume (PV, m^3)	3.0×10^5	6.3×10^5	3.0×10^5
Cumulative CO_2 at standard conditions (SC_{gas}, m^3)	3.6×10^5	7.6×10^6	7.6×10^6
Rate (m^3/day)	100	2,100	10,000
SC_{gas}/PV	12	12	12
PVI	0.06	0.06	0.06

After 1000 years of simulation, it is observed that when the volume modifier is set to 1000 and 5000, ~40.5% and ~81% of the injected CO_2 dissolved during the injection period (10 years), respectively

(**Fig. 25**). Throughout the rest of the simulation, the percentage of dissolved CO_2 remains almost the same for both cases. In contrast, only 15.4% of the injected CO_2 is in the dissolved phase for the case when no volume modifiers are used, as shown in **Figure 4**.

Appendix C. Gas Saturation and Mineral Dissolution/Precipitation Plots

C.1. Gas Saturation Plots

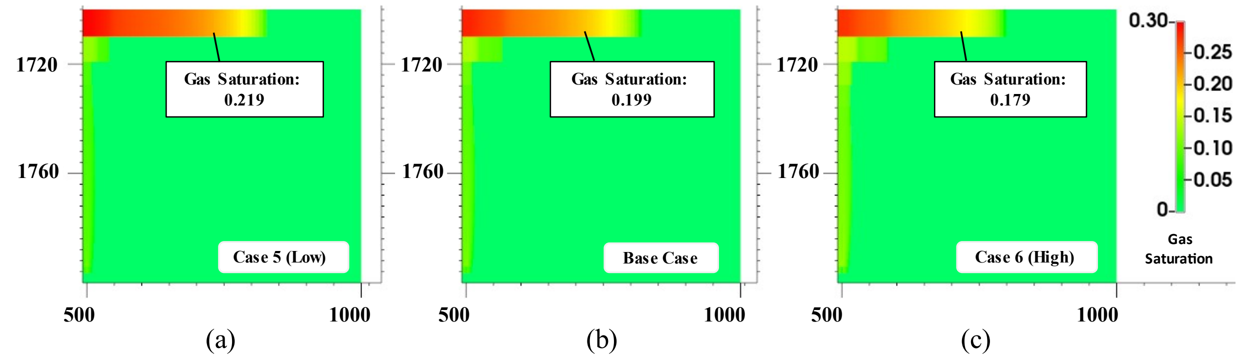

(a) (b) (c)

Figure 26. Effect of injection rate on gas saturation for (a) Case 5, (b) Base Case, (c) Case 6 after 50 years of simulation.

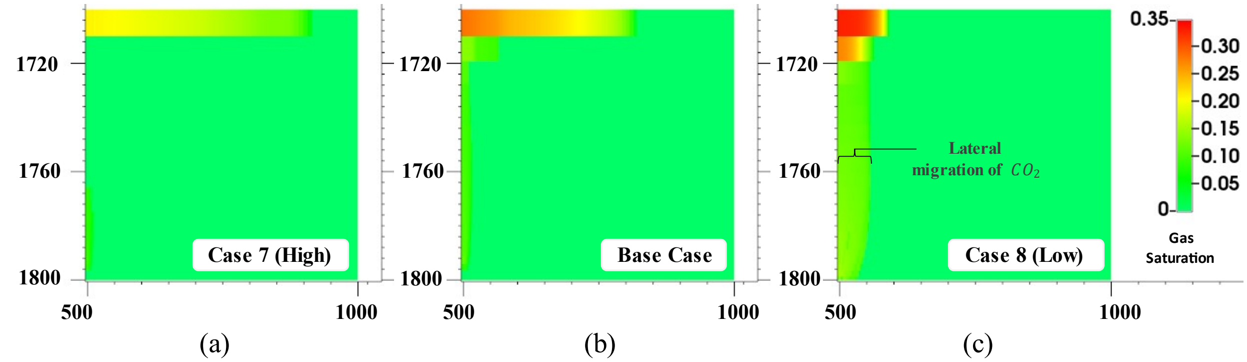

(a) (b) (c)

Figure 27. Effect of permeability on gas saturation for (a) Case 7, (b) Base Case, (c) Case 8 after 50 years of simulation.

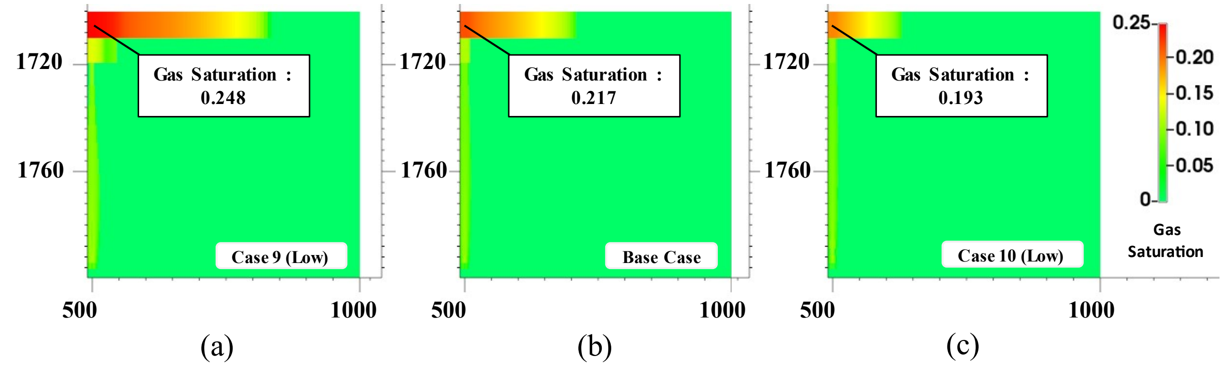

(a) (b) (c)

Figure 28. Effect of porosity on gas saturation for (a) Case 9, (b) Base Case, (c) Case 10 after 50 years of simulation.

C.2. Halite Precipitation Plots

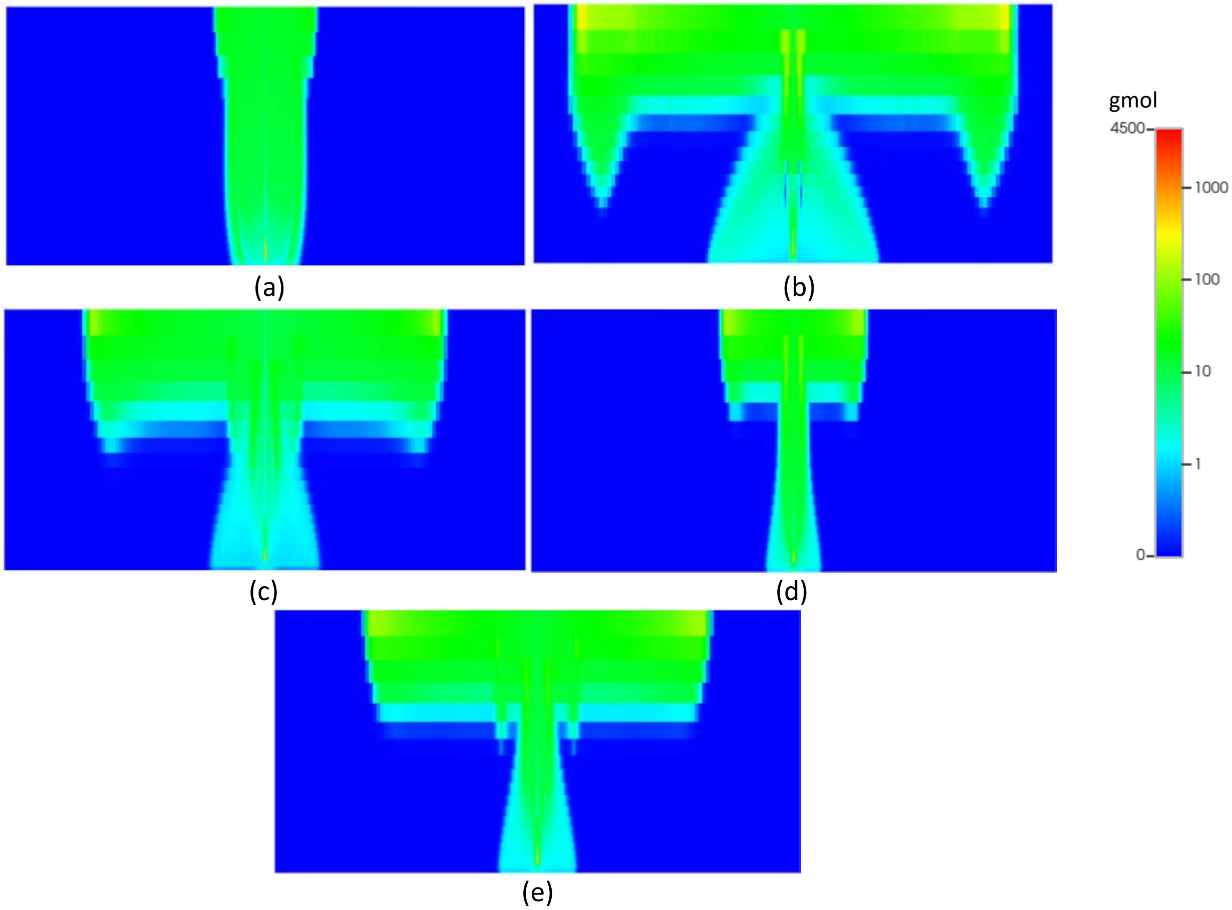

Figure 29. Halite concentration (gmol) for (a) Case 7 (low permeability), (b) Case 8 (high permeability), (c) Case 9 (low porosity) (d) Case 10 (high porosity) (e) Base case after 50 years of simulation.

C.3. Effect on initial Salt Concentration

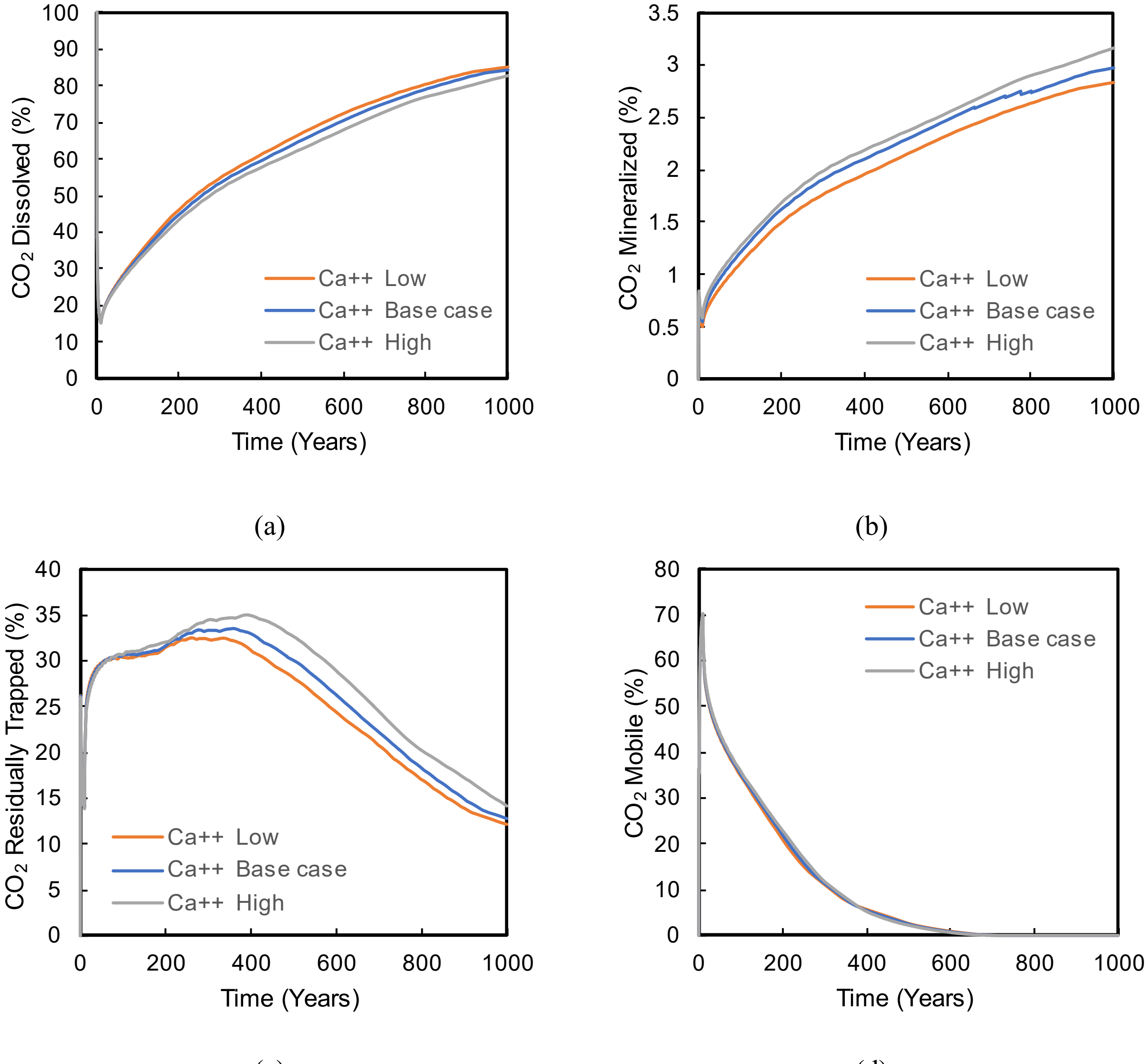

(a) (b)

(c) (d)

Figure 30. Effect of initial concentration of calcium (Ca^{++}) in CO_2 trapping by (a)dissolution, (b) mineralization, (c) residual, and (d) mobile CO_2 after 1000 years.

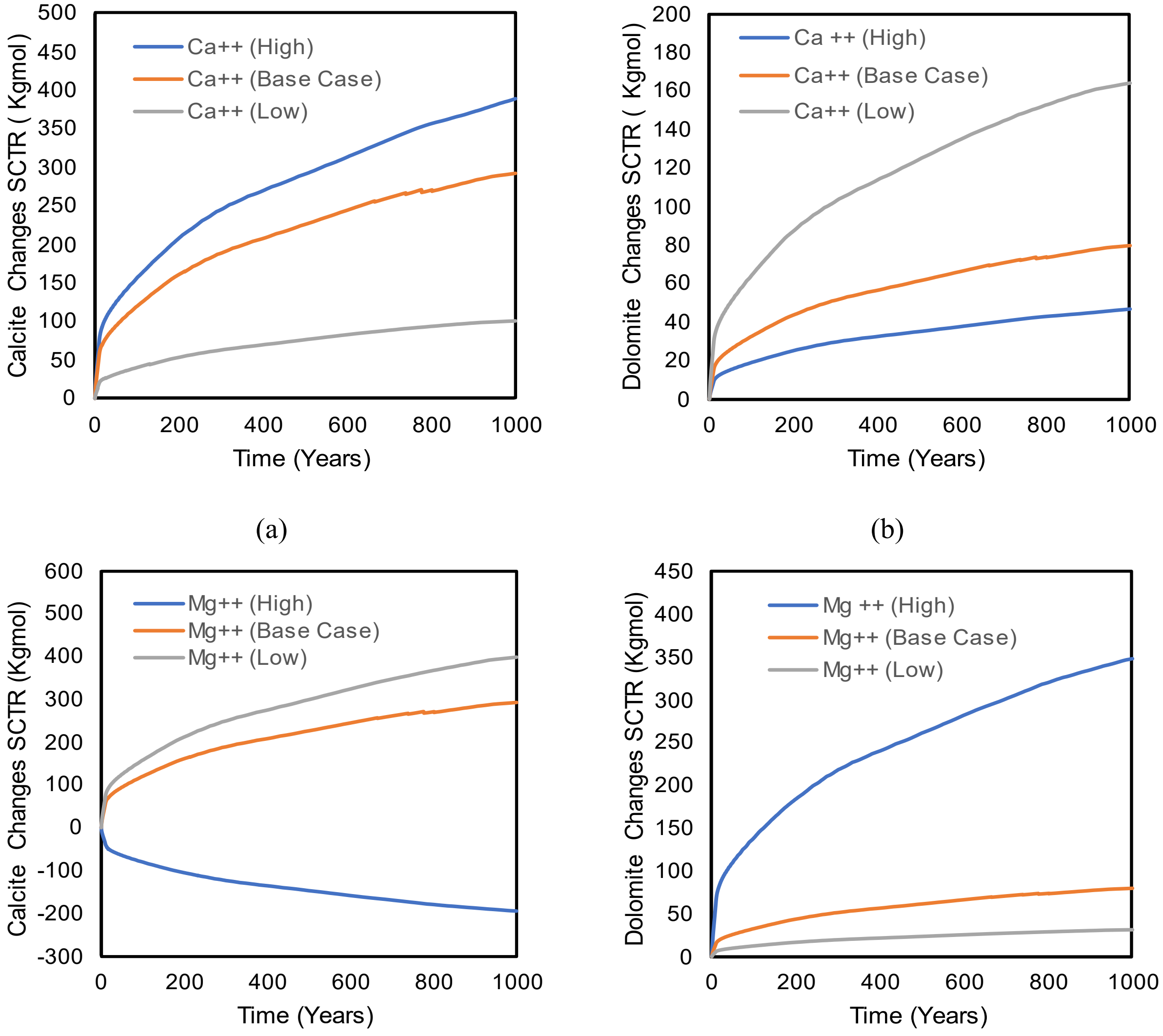

(a) (b)

(c) (d)

Figure 31. Effect of initial concentration of calcium (Ca^{++}) and magnesium (Mg^{++}) ion in calcite and dolomite dissolution/precipitation after 1000 years.

References

[1] A. Khanal, M.F. Shahriar, Optimization of CO2 Huff-n-Puff in Unconventional Reservoirs with a Focus on Pore Confinement Effects, Fluid Types, and Completion Parameters, Energies. 16 (2023) 2311. https://doi.org/10.3390/en16052311.

[2] F. Aldred, N. Gobron, J.B. Miller, K.M. Willett, R. Dunn, Global climate, Bull. Am. Meteorol. Soc. 102 (2021) S11–S142. https://doi.org/10.1175/BAMS-D-21-0098.1.

[3] IEA, Assessing the effects of economic recoveries on global energy demand and CO2 emissions in 2021., Glob. Energy Rev. 2021. (n.d.).

[4] M.F. Shahriar, A. Khanal, The current techno-economic, environmental, policy status and perspectives of sustainable aviation fuel (SAF), Fuel. 325 (2022) 124905. https://doi.org/10.1016/j.fuel.2022.124905.

A. Khanal, M. Irfan Khan, M. Fahim Shahriar, Comprehensive Parametric Study of CO2 Sequestration in Deep Saline Aquifers, Chem. Eng. Sci. (2024) 119734. https://doi.org/10.1016/j.ces.2024.119734.

[5] A. Khanal, M.F. Shahriar, Physics-Based Proxy Modeling of CO2 Sequestration in Deep Saline Aquifers, Energies. 15 (2022) 4350. https://doi.org/10.3390/en15124350.

[6] P.R.S. Masson-Delmotte, V., P. Zhai, H.-O. Pörtner, D. Roberts, J. Skea, T.M. A. Pirani, W. Moufouma-Okia, C. Péan, R. Pidcock, S. Connors, J.B.R. Matthews, Y. Chen, X. Zhou, M.I. Gomis, E. Lonnoy, and T.W. (eds. . M. Tignor, Global Warming of 1.5°C.An IPCC Special Report on the impacts of global warming of 1.5°C above pre-industrial levels and related global greenhouse gas emission pathways, in the context of strengthening the global response to the threat of climate change, IPCC, 2018. (2019).

[7] M.F. Shahriar, A. Khanal, Fundamental investigation of reactive-convective transport: Implications for long-term carbon dioxide (CO2) sequestration, Int. J. Greenh. Gas Control. 127 (2023) 103916. https://doi.org/10.1016/j.ijggc.2023.103916.

[8] M.V.B. Machado, M. Delshad, K. Sepehrnoori, Injectivity assessment for CCS field-scale projects with considerations of salt deposition, mineral dissolution, fines migration, hydrate formation, and non-Darcy flow, Fuel. 353 (2023). https://doi.org/10.1016/j.fuel.2023.129148.

[9] R. Ershadnia, S. Hajirezaie, A. Amooie, C.D. Wallace, N.I. Gershenzon, S.A. Hosseini, D.M. Sturmer, R.W. Ritzi, M.R. Soltanian, CO2 geological sequestration in multiscale heterogeneous aquifers: Effects of heterogeneity, connectivity, impurity, and hysteresis, Adv. Water Resour. 151 (2021). https://doi.org/10.1016/j.advwatres.2021.103895.

[10] L.E. Beckingham, E.H. Mitnick, C.I. Steefel, S. Zhang, M. Voltolini, A.M. Swift, L. Yang, D.R. Cole, J.M. Sheets, J.B. Ajo-Franklin, D.J. DePaolo, S. Mito, Z. Xue, Evaluation of mineral reactive surface area estimates for prediction of reactivity of a multi-mineral sediment, Geochim. Cosmochim. Acta. 188 (2016) 310–329. https://doi.org/10.1016/j.gca.2016.05.040.

[11] L. Zhang, Y. Soong, R. Dilmore, C. Lopano, Numerical simulation of porosity and permeability evolution of Mount Simon sandstone under geological carbon sequestration conditions, Chem. Geol. 403 (2015) 1–12. https://doi.org/10.1016/j.chemgeo.2015.03.014.

[12] J. Ge, X. Zhang, F. Le-Hussain, Fines migration and mineral reactions as a mechanism for CO2 residual trapping during CO2 sequestration, Energy. 239 (2022). https://doi.org/10.1016/j.energy.2021.122233.

[13] R. Gholami, A. Raza, CO2 sequestration in sandstone reservoirs: How does reactive flow alter trapping mechanisms?, Fuel. 324 (2022). https://doi.org/10.1016/j.fuel.2022.124781.

[14] T.N.V. Pavan, S.K. Govindarajan, Numerical investigations on performance of sc-CO2 sequestration associated with the evolution of porosity and permeability in low permeable saline aquifers, Geoenergy Sci. Eng. 225 (2023). https://doi.org/10.1016/j.geoen.2023.211681.

[15] C.A. Castaneda-herrera, G.W. Stevens, R.R. Haese, Review of CO2 Leakage Mitigation and Remediation Technologies, Geophys. Monogr. Ser. 238 (2018) 327–337. https://doi.org/10.1002/9781119118657.ch16.

[16] T. Xiao, H. Xu, N. Moodie, R. Esser, W. Jia, L. Zheng, J. Rutqvist, B. McPherson, Chemical-Mechanical Impacts of CO 2 Intrusion Into Heterogeneous Caprock, Water Resour. Res. 56 (2020). https://doi.org/10.1029/2020WR027193.

[17] S. Mohd Amin, D.J. Weiss, M.J. Blunt, Reactive transport modelling of geologic CO2 sequestration in saline aquifers: The influence of pure CO2 and of mixtures of CO2 with CH4 on the sealing capacity of cap rock at 37°C and 100bar, Chem. Geol. 367 (2014) 39–50. https://doi.org/10.1016/j.chemgeo.2014.01.002.

[18] A.G. Ilgen, M. Aman, D.N. Espinoza, M.A. Rodriguez, J.M. Griego, T.A. Dewers, J.D. Feldman, T.A. Stewart, R.C. Choens, J. Wilson, Shale-brine-CO2 interactions and the long-term stability of carbonate-rich shale caprock, Int. J. Greenh. Gas Control. 78 (2018) 244–253. https://doi.org/10.1016/j.ijggc.2018.07.002.

[19] R. Shiraki, T.L. Dunn, Experimental study on water–rock interactions during CO2 flooding in the Tensleep Formation, Wyoming, USA, Appl. Geochemistry. 15 (2000) 265–279. https://doi.org/10.1016/S0883-2927(99)00048-7.

[20] S.G. Sayegh, F.F. Krause, M. Girard, C. DeBree, Rock/Fluid Interactions of Carbonated Brines in a Sandstone Reservoir: Pembina Cardium, Alberta, Canada, SPE Form. Eval. 5 (1990) 399–405. https://doi.org/10.2118/19392-PA.

[21] S.A. Carroll, W.W. McNab, Z. Dai, S.C. Torres, Reactivity of Mount Simon sandstone and the Eau Claire shale under CO 2 storage conditions, Environ. Sci. Technol. 47 (2013) 252–261. https://doi.org/10.1021/es301269k.

[22] F. Liu, P. Lu, C. Zhu, Y. Xiao, Coupled reactive flow and transport modeling of CO2 sequestration in the Mt. Simon sandstone formation, Midwest U.S.A., Int. J. Greenh. Gas Control. 5 (2011) 294–307. https://doi.org/10.1016/j.ijggc.2010.08.008.

[23] D. Edem, M. Abba, A. Nourian, M. Babaie, Z. Naeem, Experimental Investigation of the Extent of the Impact of Halite Precipitation on CO2 Injection in Deep Saline Aquifers, in: Day 1 Tue, December 01, 2020, SPE, 2020. https://doi.org/10.2118/200632-MS.

[24] M. Babaei, Integrated Carbon Sequestration–Geothermal Heat Recovery: Performance Comparison Between Open and Close Systems, Transp. Porous Media. 126 (2019) 249–273. https://doi.org/10.1007/s11242-018-1042-1.

[25] T. Giorgis, M. Carpita, A. Battistelli, 2D modeling of salt precipitation during the injection of dry CO2 in a depleted gas reservoir, Energy Convers. Manag. 48 (2007) 1816–1826. https://doi.org/10.1016/j.enconman.2007.01.012.

[26] A. Khanal, R. Weijermars, Distinguishing Fracture Conductivity and Fracture Flux: A Systematic Investigation of Individual Fracture Contribution to Well Productivity, in: Proc. 8th Unconv. Resour. Technol. Conf., American Association of Petroleum Geologists, Tulsa, OK, USA, 2020. https://doi.org/10.15530/urtec-2020-2176.

[27] A. Khanal, R. Weijermars, Comparison of Flow Solutions for Naturally Fractured Reservoirs Using Complex Analysis Methods (CAM) and Embedded Discrete Fracture Models (EDFM): Fundamental Design Differences and Improved Scaling Method, Geofluids. 2020 (2020) 1–20. https://doi.org/10.1155/2020/8838540.

[28] A. Khanal, R. Weijermars, Pressure depletion and drained rock volume near hydraulically fractured parent and child wells, J. Pet. Sci. Eng. 172 (2019). https://doi.org/10.1016/j.petrol.2018.09.070.

[29] M. Khoshghadam, A. Khanal, W.J. Lee, Numerical study of production mechanisms and gas-oil ratio behavior of liquid-rich shale oil reservoirs, in: Proc. - SPE Annu. Tech. Conf. Exhib., 2015.

[30] S. Parvin, M. Masoudi, A. Sundal, R. Miri, Continuum scale modelling of salt precipitation in the context of CO2 storage in saline aquifers with MRST compositional, Int. J. Greenh. Gas Control. 99 (2020) 103075. https://doi.org/10.1016/j.ijggc.2020.103075.

[31] R. Miri, R. van Noort, P. Aagaard, H. Hellevang, New insights on the physics of salt precipitation during injection of CO2 into saline aquifers, Int. J. Greenh. Gas Control. 43 (2015) 10–21.

https://doi.org/10.1016/j.ijggc.2015.10.004.

[32] R. Juanes, E.J. Spiteri, F.M. Orr, M.J. Blunt, Impact of relative permeability hysteresis on geological CO 2 storage, Water Resour. Res. 42 (2006). https://doi.org/10.1029/2005WR004806.

[33] B. Pan, K. Liu, B. Ren, M. Zhang, Y. Ju, J. Gu, X. Zhang, C.R. Clarkson, K. Edlmann, W. Zhu, S. Iglauer, Impacts of relative permeability hysteresis, wettability, and injection/withdrawal schemes on underground hydrogen storage in saline aquifers, Fuel. 333 (2023). https://doi.org/10.1016/j.fuel.2022.126516.

[34] R. Sedaghatinasab, S. Kord, J. Moghadasi, A. Soleymanzadeh, Relative Permeability Hysteresis and Capillary Trapping during CO2 EOR and Sequestration, Int. J. Greenh. Gas Control. 106 (2021). https://doi.org/10.1016/j.ijggc.2021.103262.

[35] T. Akai, T. Kuriyama, S. Kato, H. Okabe, Numerical modelling of long-term CO2 storage mechanisms in saline aquifers using the Sleipner benchmark dataset, Int. J. Greenh. Gas Control. 110 (2021) 103405. https://doi.org/10.1016/j.ijggc.2021.103405.

[36] R. Guo, L. Dalton, D. Crandall, J. McClure, H. Wang, Z. Li, C. Chen, Role of heterogeneous surface wettability on dynamic immiscible displacement, capillary pressure, and relative permeability in a CO2-water-rock system, Adv. Water Resour. 165 (2022). https://doi.org/10.1016/j.advwatres.2022.104226.

[37] M. Delshad, X. Kong, R. Tavakoli, S.A. Hosseini, M.F. Wheeler, Modeling and simulation of carbon sequestration at Cranfield incorporating new physical models, Int. J. Greenh. Gas Control. 18 (2013) 463–473. https://doi.org/10.1016/j.ijggc.2013.03.019.

[38] Y. Zhang, H.R. Lashgari, K. Sepehrnoori, Y. Di, Effect of capillary pressure and salinity on CO 2 solubility in brine aquifers, Int. J. Greenh. Gas Control. 57 (2017) 26–33. https://doi.org/10.1016/j.ijggc.2016.12.012.

[39] G.J. Moridis, M.T. Reagan, T. Huang, T.A. Blasingame, Practical Aspects and Implications of Long-Term CO2 Sequestration in Saline Aquifers Using Vertical Wells, (2023). https://doi.org/10.2118/213168-ms.

[40] N. Smith, P. Boone, A. Oguntimehin, G. van Essen, R. Guo, M.A. Reynolds, L. Friesen, M.-C. Cano, S. O'Brien, Quest CCS facility: Halite damage and injectivity remediation in CO2 injection wells, Int. J. Greenh. Gas Control. 119 (2022) 103718. https://doi.org/10.1016/j.ijggc.2022.103718.

[41] B. Liu, F. Zhao, J. Xu, Y. Qi, Experimental Investigation and Numerical Simulation of CO2–Brine–Rock Interactions during CO2 Sequestration in a Deep Saline Aquifer, Sustainability. 11 (2019) 317. https://doi.org/10.3390/su11020317.

[42] L. Ang, L. Yongming, C. Xi, Z. Zhongyi, P. Yu, Review of CO2 sequestration mechanism in saline aquifers, Nat. Gas Ind. B. (2022). https://doi.org/10.1016/j.ngib.2022.07.002.

[43] S. Luo, R. Xu, P. Jiang, Effect of reactive surface area of minerals on mineralization trapping of CO 2 in saline aquifers, Pet. Sci. 9 (2012) 400–407. https://doi.org/10.1007/s12182-012-0224-7.

[44] A.N. Awolayo, C.T. Laureijs, J. Byng, A.J. Luhmann, R. Lauer, B.M. Tutolo, Mineral surface area accessibility and sensitivity constraints on carbon mineralization in basaltic aquifers, Geochim. Cosmochim. Acta. 334 (2022) 293–315. https://doi.org/10.1016/j.gca.2022.08.011.

[45] W. Jia, T. Xiao, Z. Wu, Z. Dai, B. McPherson, Impact of mineral reactive surface area on forecasting geological carbon sequestration in a co2-eor field, Energies. 14 (2021) 1–22.

https://doi.org/10.3390/en14061608.

[46] L. Nghiem, P. Sammon, J. Grabenstetter, H. Ohkuma, Modeling CO2 Storage in Aquifers with a Fully-Coupled Geochemical EOS Compositional Simulator, in: Proc. SPE/DOE Symp. Improv. Oil Recover., Society of Petroleum Engineers, 2004. https://doi.org/10.2523/89474-MS.

[47] A.M. Norouzi, M. Babaei, W.S. Han, K.-Y. Kim, V. Niasar, CO2-plume geothermal processes: A parametric study of salt precipitation influenced by capillary-driven backflow, Chem. Eng. J. 425 (2021) 130031. https://doi.org/10.1016/j.cej.2021.130031.

[48] V. Smith, P. Jaques, Illinois Basin – Decatur Project pre-injection microseismic analysis, Int. J. Greenh. Gas Control. 54 (2016) 362–377. https://doi.org/10.1016/j.ijggc.2015.12.004.

[49] S. Gollakota, S. McDonald, Commercial-scale CCS Project in Decatur, Illinois – Construction Status and Operational Plans for Demonstration, Energy Procedia. 63 (2014) 5986–5993. https://doi.org/10.1016/j.egypro.2014.11.633.

[50] R.A. Bauer, R. Will, S. E. Greenberg, S.G. Whittaker, Illinois Basin–Decatur Project, in: Geophys. Geosequestration, Cambridge University Press, 2019: pp. 339–370. https://doi.org/10.1017/9781316480724.020.

[51] D.M. Labotka, S. V. Panno, R.A. Locke, J.T. Freiburg, Isotopic and geochemical characterization of fossil brines of the Cambrian Mt. Simon Sandstone and Ironton-Galesville Formation from the Illinois Basin, USA, Geochim. Cosmochim. Acta. 165 (2015) 342–360. https://doi.org/10.1016/j.gca.2015.06.013.

[52] J.T. Freiburg, D.G. Morse, H.E. Leetaru, R.P. Hoss, Q. Yan, A Depositional and Diagenetic Characterization of the Mt . Simon Sandstone at the Illinois Basin - Decatur Project Carbon Capture and Storage Site , Decatur , Illinois , USA, (2014) 73.

[53] S.C.M. Krevor, R. Pini, L. Zuo, S.M. Benson, Relative permeability and trapping of CO 2 and water in sandstone rocks at reservoir conditions, Water Resour. Res. 48 (2012) 1–16. https://doi.org/10.1029/2011WR010859.

[54] B. Shabani, P. Lu, R. Kammer, C. Zhu, Effects of Hydrogeological Heterogeneity on CO2 Migration and Mineral Trapping: 3D Reactive Transport Modeling of Geological CO2 Storage in the Mt. Simon Sandstone, Indiana, USA, Energies. 15 (2022) 2171. https://doi.org/10.3390/en15062171.

[55] Y. Soong, B.H. Howard, S.W. Hedges, I. Haljasmaa, R.P. Warzinski, G. Irdi, T.R. McLendon, CO2 Sequestration in Saline Formation, Aerosol Air Qual. Res. 14 (2014) 522–532. https://doi.org/10.4209/aaqr.2013.06.0195.

[56] J.T. Freiburg, M. Amer, K. Henkel, K. Wemmer, G.H. Grathoff, Illitization in the Mt. Simon Sandstone, Illinois Basin, USA: Implications for carbon dioxide storage, Mar. Pet. Geol. 146 (2022) 105963. https://doi.org/10.1016/j.marpetgeo.2022.105963.

[57] E.O. Munson, G.R.L. Chalmers, R.M. Bustin, K. Li, Utilizing smear mounts for X-ray diffraction as a fully quantitative approach in rapidly characterizing the mineralogy of shale gas reservoirs, J. Unconv. Oil Gas Resour. 14 (2016) 22–31. https://doi.org/10.1016/j.juogr.2016.01.001.

[58] G.P.D. De Silva, P.G. Ranjith, M.S.A. Perera, Geochemical aspects of CO2 sequestration in deep saline aquifers: A review, Fuel. 155 (2015) 128–143. https://doi.org/10.1016/j.fuel.2015.03.045.

[59] J.L. Palandri, Y.K. Kharaka, A compilation of rate parameters of water-mineral interaction kinetics for application to geochemical modeling, Menlo Park, California, 2004.

http://www.dtic.mil/cgi-bin/GetTRDoc?Location=U2&doc=GetTRDoc.pdf&AD=ADA440035.

[60] S.V. Golubev, P. Bénézeth, J. Schott, J.L. Dandurand, A. Castillo, Siderite dissolution kinetics in acidic aqueous solutions from 25 to 100 °C and 0 to 50 atm pCO2, Chem. Geol. 265 (2009) 13–19. https://doi.org/10.1016/j.chemgeo.2008.12.031.

[61] Dullien and Francis AL, Porous media: fluid transport and pore structure, Academic Press Limited, 2012.

[62] A. Kumar, R. Ozah, M. Noh, G.A. Pope, S. Bryant, K. Sepehrnoori, L.W. Lake, Reservoir Simulation of CO2 Storage in Deep Saline Aquifers, SPE J. 10 (2005) 336–348. https://doi.org/10.2118/89343-PA.

[63] C.S. Land, Calculation of Imbibition Relative Permeability for Two- and Three-Phase Flow From Rock Properties, Soc. Pet. Eng. J. 8 (1968) 149–156. https://doi.org/10.2118/1942-PA.

[64] T. Kogure, Y. Zhang, O. Nishizawa, Z. Xue, Changes in migration mode of brine and supercritical CO2 in imbibition process under steady flow state of very slow fluid velocities, Geophys. J. Int. 214 (2018) 1413–1425. https://doi.org/10.1093/gji/ggy210.

[65] S. Iglauer, C.H. Pentland, A. Busch, CO 2 wettability of seal and reservoir rocks and the implications for carbon geo-sequestration, Water Resour. Res. 51 (2015) 729–774. https://doi.org/10.1002/2014WR015553.

[66] C.H. Pentland, S.. Iglauer, O.. Gharbi, K.. Okada, T.. Suekane, The influence of pore space geometry on the entrapment of carbon dioxide by capillary forces, in: SPE Asia Pacific Oil Gas Conf. Exhib., SPE, 2012. https://doi.org/10.2118/158516-MS.

[67] S. Iglauer, W. Wülling, C.H. Pentland, S.K. Al-Mansoori, M.J. Blunt, Capillary-Trapping Capacity of Sandstones and Sandpacks, SPE J. 16 (2011) 778–783. https://doi.org/10.2118/120960-PA.

[68] E.A. Al-Khdheeawi, D.S.M. Mahdi, M. Ali, S. Iglauer, A. Barifcani, Reservoir Scale Porosity-Permeability Evolution in Sandstone Due to CO2 Geological Storage, SSRN Electron. J. (2021). https://doi.org/10.2139/ssrn.3818887.

[69] G. Cui, Y. Wang, Z. Rui, B. Chen, S. Ren, L. Zhang, Assessing the combined influence of fluid-rock interactions on reservoir properties and injectivity during CO2 storage in saline aquifers, Energy. 155 (2018) 281–296. https://doi.org/10.1016/j.energy.2018.05.024.

[70] F. Liu, P. Lu, C. Griffith, S.W. Hedges, Y. Soong, H. Hellevang, C. Zhu, CO2–brine–caprock interaction: Reactivity experiments on Eau Claire shale and a review of relevant literature, Int. J. Greenh. Gas Control. 7 (2012) 153–167. https://doi.org/10.1016/j.ijggc.2012.01.012.

[71] E.J. Spiteri, R. Juanes, Impact of relative permeability hysteresis on the numerical simulation of WAG injection, J. Pet. Sci. Eng. 50 (2006) 115–139. https://doi.org/10.1016/j.petrol.2005.09.004.

[72] M.F. Shahriar, A. Khanal, Effect of Formation Heterogeneity on CO 2 Dissolution in Subsurface Porous Media, ACS Earth Sp. Chem. 7 (2023) 2073–2090. https://doi.org/10.1021/acsearthspacechem.3c00175.

[73] M. Abdelaal, M. Zeidouni, I.J. Duncan, Effects of injection well operation conditions on CO2 storage capacity in deep saline aquifers, Greenh. Gases Sci. Technol. 11 (2021) 734–749. https://doi.org/10.1002/ghg.2076.

[74] P. Bolourinejad, P. Shoeibi Omrani, R. Herber, Effect of reactive surface area of minerals on

mineralization and carbon dioxide trapping in a depleted gas reservoir, Int. J. Greenh. Gas Control. 21 (2014) 11–22. https://doi.org/10.1016/j.ijggc.2013.11.020.

[75] H. Hellevang, V.T.H. Pham, P. Aagaard, Kinetic modelling of CO2–water–rock interactions, Int. J. Greenh. Gas Control. 15 (2013) 3–15. https://doi.org/10.1016/j.ijggc.2013.01.027.

[76] D.-Y. Peng, D.B. Robinson, A New Two-Constant Equation of State, Ind. Eng. Chem. Fundam. 15 (1976) 59–64. https://doi.org/10.1021/i160057a011.

[77] A.M. Rowe, J.C.S. Chou, Pressure-volume-temperature-concentration relation of aqueous sodium chloride solutions, J. Chem. Eng. Data. 15 (1970) 61–66. https://doi.org/10.1021/je60044a016.

[78] J. Kestin, H.E. Khalifa, R.J. Correia, Tables of the dynamic and kinematic viscosity of aqueous NaCl solutions in the temperature range 20–150 °C and the pressure range 0.1–35 MPa, J. Phys. Chem. Ref. Data. 10 (1981) 71–88. https://doi.org/10.1063/1.555641.

[79] Y.-K. Li, L.X. Nghiem, Phase equilibria of oil, gas and water/brine mixtures from a cubic equation of state and henry’s law, Can. J. Chem. Eng. 64 (1986) 486–496. https://doi.org/10.1002/cjce.5450640319.

[80] A.H. Harvey, Semiempirical correlation for Henry’s constants over large temperature ranges, AIChE J. 42 (1996) 1491–1494. https://doi.org/10.1002/aic.690420531.

[81] Stephen D. Cramer, The Solubility of Methane, Carbon Dioxide and Oxygen in Brines from 0 degree to 300 degree Celcius, US Bureau of Mines, Report No. 8706, USA, 16 pp., n.d.

[82] R.J. Bakker, Package FLUIDS 1. Computer programs for analysis of fluid inclusion data and for modelling bulk fluid properties, Chem. Geol. 194 (2003) 3–23. https://doi.org/10.1016/S0009-2541(02)00268-1.

[83] Computer Modeling Group Ltd., GEM User Guide, (2022).

[84] F.S.M. L. Canjar, Thermodynamic properties and reduced correlations for gases, Gulf Publishing Company, 1967.

[85] W. Wagner, A. Pruss, International Equations for the Saturation Properties of Ordinary Water Substance. Revised According to the International Temperature Scale of 1990. Addendum to J. Phys. Chem. Ref. Data 16 , 893 (1987), J. Phys. Chem. Ref. Data. 22 (1993) 783–787. https://doi.org/10.1063/1.555926.

[86] R. Azin, M. Mahmoudy, S. Raad, S. Osfouri, Measurement and modeling of CO2 diffusion coefficient in Saline Aquifer at reservoir conditions, Open Eng. 3 (2013). https://doi.org/10.2478/s13531-012-0069-2.

[87] Craig M. Bethke, Geochemical Reaction Modeling: Concepts and Applications, Oxford University Press, 1996.

[88] Craig M. Bethke, Geochemical and Biogeochemical Reaction Modeling, Cambridge University Press, n.d.

[89] M. Gamal Rezk, A. Farid Ibrahim, A.R. Adebayo, Influence of impurities on reactive transport of CO2 during geo-sequestration in saline aquifers, Fuel. 344 (2023). https://doi.org/10.1016/j.fuel.2023.127994.

[90] H. Firoozmand, Y. Leonenko, An analytical approach to the technical and economical optimization of CO2 sequestration in saline aquifers with simultaneous brine production, J. Clean. Prod. 372 (2022). https://doi.org/10.1016/j.jclepro.2022.133453.

A. Khanal, M. Irfan Khan, M. Fahim Shahriar, Comprehensive Parametric Study of CO2 Sequestration in Deep Saline Aquifers, Chem. Eng. Sci. (2024) 119734. https://doi.org/10.1016/j.ces.2024.119734.

[91] F. Qin, L.E. Beckingham, The impact of mineral reactive surface area variation on simulated mineral reactions and reaction rates, Appl. Geochemistry. 124 (2021) 104852. https://doi.org/10.1016/j.apgeochem.2020.104852.

[92] S. Galí, C. Ayora, P. Alfonso, E. Tauler, M. Labrador, Kinetics of dolomite–portlandite reaction, Cem. Concr. Res. 31 (2001) 933–939. https://doi.org/10.1016/S0008-8846(01)00499-9.

[93] I. Ávila, P.M. Crnkovic, F.E. Milioli, K.H. Luo, Investigation of the pore blockage of a Brazilian dolomite during the sulfation reaction, Appl. Surf. Sci. 258 (2012) 3532–3539. https://doi.org/10.1016/j.apsusc.2011.11.108.

[94] O.S. Pokrovsky, J.A. Mielczarski, O. Barres, J. Schott, Surface Speciation Models of Calcite and Dolomite/Aqueous Solution Interfaces and Their Spectroscopic Evaluation, Langmuir. 16 (2000) 2677–2688. https://doi.org/10.1021/la980905e.